The Dissertation Committee for Mingzhou Jin Certifies that this is the approved version of the following Dissertation:

High Sensitivity Infrared Nano-Spectroscopy in Ambient and Water Environment

Committee:

Mikhail A. Belkin, Supervisor

Edward Yu

Deji Akinwande

Lauren Webb

Alejandro De Lozanne

High Sensitivity Infrared Nano-Spectroscopy in Ambient and Water Environment

by

Mingzhou Jin

Dissertation

Presented to the Faculty of the Graduate School of

The University of Texas at Austin

in Partial Fulfillment

of the Requirements

for the Degree of

DOCTOR OF PHILOSOPHY

The University of Texas at Austin

December 2018

Acknowledgements

First and foremost, I would like to express my special appreciation for my advisor and mentor, Professor Mikhail A. Belkin. I could not have imagined to have a better advisor for my PhD study. His endless passion, creativity and incisiveness in science has guided and supported me from my first day at UT Austin. I am always amazed at his clear physical pictures and innovative experimental resolutions. Apart from his extraordinary talent and diligence, his character of being truthful, patient and open-minded to everyone has influenced me at all times.

I would like to thank Professor Edward T. Yu, Professor Deji Akinwande, Professor Lauren Webb and Professor Alex de Lozanne for serving on my qualifying examination committee and dissertation committee. Their insightful comments and invaluable advice helped to shape my final dissertation.

I am grateful to the past and present members in Belkin's group. I feel lucky to have worked with Dr. Feng Lu on the AFM-IR project. His solid understanding in Physics and generous assistance has introduced me to the research of AFM-IR at the beginning of my graduate years. I would like to thank Dr. Seungyong Jung and Jaehyun Kim for their expertise in both the theory and hands-on experiments of quantum cascade lasers. Dr. Yifan Jiang helped me in nano-fabrication and optical system alignment. Nish Nookala has given me valuable advice on fabrication and simulation of nano-antennas. I would like to thank all the other colleagues: Dr. Aiting Jiang, Dr. Daniele Palaferri, Dr. Min Jang, Dr. Jongwon Lee, Dr. Karun Vijayraghavan, Kevin Zhang, Jiaming Xu, Jialin Mei, Yingnan Liu.

I am also grateful to our collaborators from other research groups and industry. Dr. Georg Ramer, previously at Vienna University of Technology and now at NIST, helped to build our integrated QCL control and data acquisition software. Besides, I benefit a lot from the discussion with Dr. Craig Prater and Kevin Kjoller in Photothermal Spectroscopy Corp.

Last but not least, I would like to thank my parents for giving me the opportunity of choosing the career I love, and teaching me to think from a different perspective. And thanks to my friends and colleagues for their warm encouragement, continued patience and everlasting support.

Abstract

High Sensitivity Infrared Nano-Spectroscopy in Ambient and Water Environment

Mingzhou Jin, PhD

The University of Texas at Austin, 2018

Supervisor: Mikhail A. Belkin

Mid-infrared (mid-IR) vibrational spectroscopy is a universal label–free tool for identifying molecular compounds via their 'fingerprint' vibrational absorption lines. Infrared nano-spectroscopies with nanoscale spatial resolution can reveal the chemical and physical properties at a few nanometers, and several scanning probe techniques[1–9] have been developed to address this need. Among these methods, AFM-IR and scattering nearfield scanning microscopy (s-NSOM) have produced outstanding results in mid-IR and far-IR spectral range.

In this thesis, a set of experiments are presented, which have substantially improved AFM-IR in terms of the sensitivity and resolution, and have implemented the system for operation under different conditions. We demonstrated high-sensitivity AFM-IR on monolayer molecules via molecular expansion force. AFM-IR microscopy and spectroscopy is also demonstrated on thin films in aqueous environment, which offers the possibility of *in vivo* studies of biological samples using IR nanospectroscopies[10]. Apart from AFM-IR, s-NSOM imaging using the self-mixing detection in mid-IR quantum

cascade lasers (QCL) is also presented in this dissertation. The phase and amplitude of the scattered light field can be analyzed from the voltage signal on the QCL, without the need of external-cavity interferometric optical setup.

Table of Contents

List of Tables

List of Figures

Chapter 1 Introduction

Nanoscience and nanotechnology have been applied to a wide range of topics, including material science, life science, clinical medicine, semiconductor nano-devices and environmental monitoring. The continuous development in nanotechnology cannot do without the advancement in the nano-tools for characterization of the sample composition and properties.

The task of developing analytical tools for nanoscale characterization is challenging for three reasons. First of all, the limited detection sensitivity. Small volume of material produces small signal, regardless of the type of the signal (optical, electrical, heat…), which makes the detection sensitivity a critical issue. Low detection sensitivity seriously deteriorates the measurement accuracy and efficiency, and restrains our ability of acquiring significant sample information in a short time period. The challenge lies in developing weak signal enhancement and noise reduction methods. The second challenge is the limitation in detection resolution. After the excitation and collection of the sample signal, a successful technique should be able to extract specific local information from that of closely-spaced areas. However, the detection resolution is limited in different techniques that requires additional effort to overcome. Last but not least, the versatility of the nano-tools on different samples and in various conditions are limited. For example, soft samples like tissues and cell membranes may be damaged at the focal spot of high power laser pulses, due to the abrupt and inhomogeneous temperature increase, which makes it difficult for repeated experiments on biological samples. Another example is the dramatic decrease in the performance of atomic force microscopes (AFM) in aqueous environment, where

some important chemistry and biological phenomena in liquid cannot be characterized properly.

To overcome the ubiquitous challenges among analytical nanotechnology tools, novel ideas and techniques are introduced and carried out constantly over the past decades.

1.1 VIBRATIONAL SPECTROSCOPIES

"Fingerprint" vibrational frequencies of molecular bonds have been a universal label-free standard for chemical identification and characterization, on which varieties of vibrational spectroscopy methods have been developed. These methods provide broad types of analytical tools, from absorption to scattering and dispersion techniques, covering the spectral range of far-infrared (IR), mid-IR, near-IR and visible range. Among them, the most widely-used methods are IR absorption spectroscopy and Raman spectroscopy.

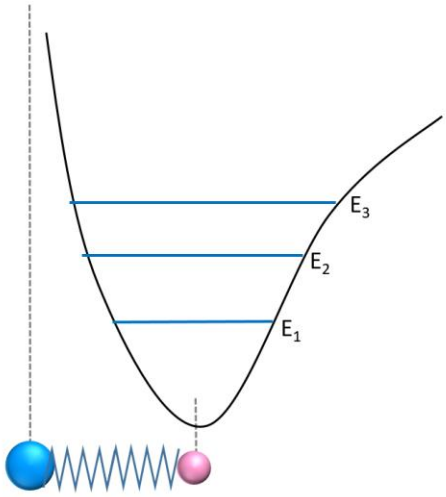

Figure1.1: Morse potential model of diatom system.

The potential well of diatomic interactions can be approximated with the Morse potential model (Figure 1.1), where the vibrational energies and eigenstates can be found by solving the quantum equations. In a multi-atom molecule, the interatomic interaction creates a set of vibrational states that are unique to each chemical. Transition between two vibrational states will cause absorption or emission of photons of the energy difference between the two states. For most organic compositions, the direct transition energies mostly fall in the range of mid-IR (wavelength range 2.5-25 μm) to far-IR region (wavelength range 30 μm – 300 μm). Apart from direct absorption, light-molecule interaction also causes inelastic scattering, or in other words, "Raman scattering", where the energy difference between excitation light and scattered light corresponds to a set of vibrational states. Based on the principle, IR absorption spectroscopy and Raman spectroscopy are invented and become commonly used tools for characterization of material composition and properties. Surface Enhanced Raman spectroscopy (SERS) was the first to achieve vibrational spectroscopy with single molecule sensitivity[11,12]. But the disadvantage of Raman spectroscopy is the small signal. Raman scattering is a weak effect, with the molecular scattering cross section at 10^{-30}~10^{-25}cm^{-2}.[13] High optical power input and complex sample preparation with silver colloidal particles is required for signal enhancement, which narrows the types of suitable samples. On the other hand, the molecule IR absorption cross section is 10^{-21}~10^{-18}cm^{-2}, which indicates a much higher efficiency in light-molecule interaction. Since the invention of Fourier Transform IR spectroscopy in the 1950s, new techniques have been brought into the IR family, for example, reflection absorption IR spectroscopy (RAIRS), diffusive reflectance IR spectroscopy (DRIFTS), and attenuated total reflectance (ATR), surface-enhanced infrared absorption (SEIRA).

However, given the numerical aperture NA (NA≤1), the resolution of all the far-field optical imaging systems cannot be finer than far-field diffraction limit δ:

$$\delta = \frac{\lambda}{2NA} \tag{1.1}$$

which is on the order of a few microns depending on the wavelength. As a result, it is challenging to measure spectra on nano-structured samples, for instance, DNA strands, block copolymers, protein fiber, plasmonic nanostructures and *etc*.

To address the need of performing vibrational spectroscopy with nanometer spatial resolution, several scanning probe based nearfield nano-spectroscopies are developed.

1.2 NEAR-FIELD NANO-SPECTROSCOPIES

The early eighties has witnessed the birth of a new generation of nano-imaging systems based on detection and use of the interaction between a scanning probe and the sample surface. In 1981, the first member of this family, the scanning tunneling microscope (STM), is invented by Binnig and Rohrer in the Research Center of IBM[14,15]. A few years later, the atomic force microscopy is demonstrated by Binnig, Quate and Gerber[16].

The success of scanning probe imaging systems led to the invention of the near-field scanning optical microscopes (NSOM) in 1986[17,18]. It uses a tapered hollow metal waveguide probe with a tiny aperture at the tip apex, and bring the probe close to the sample surface to break the far-field diffraction limit and exploit near-field evanescent wave. This technique is later more specifically termed as aperture-NSOM, in order to distinguish itself

from scattering-NSOM (or apertureless-NSOM) which does not require an aperture probe for light illumination or detection. With aperture-NSOM, a spatial resolution of up to λ/10 has been reported[19,20]. Vibrational spectroscopy methods including Raman and IR techniques also start to join the aperture-NSOM family, which prompt the development of the Raman NSOM[21] and the scanning near-field Infrared microscope (SNIM)[22–26]. Nano-imaging of biological relevant samples under water environment became popular with aperture-NSOM[26,27]. However, the intrinsic cut-off effect and strong heating effect near the aperture eventually prevented it from reaching higher spatial resolution and image contrast.

As an alternative approach, the scattering-NSOM (s-NSOM) is proposed and demonstrated[28–30].The idea of s-NSOM comes from the radioelectronics, where a simple metallic wire antenna couples waves from free space and scatter light as a near-field subwavelength dipole[31]. By analyzing the amplitude and phase of the scattered field, one can calculate the local sample permittivity or local optical density of states. In this case, the spatial resolution is only limited by the size of the near-field probe. An impressive λ/100 spatial resolution was achieved with the s-NSOM configuration at 10 μm IR wavelength[32] in 2000. After that, the spatial resolution of IR s-NSOM systems is reported below 10 nm in the lateral direction[33,34]. The implementation of heterodyne[33,35,36] and homodyne[36] detection setup in IR s-NSOM further improved the detection sensitivity and accuracy of the technique, which has allowed us to investigate a wide variety of important samples and physics phenomena[37]. For example, the graphene surface plasmons was launched and captured with IR s-NSOM in monolayer graphene sheet in 2012[38,39], which was a milestone for experimental studies of surface plasmon polaritons in 2-d materials. Besides, the incorporation of broad-band IR sources including FTIR[2,3] , optical parametric

oscillators (OPOs)[37] and tunable quantum cascade lasers (QCLs)[5,10,40,41] has greatly extended the IR spectral range of s-NSOM. At the same time, tip enhanced Raman spectroscopy (TERS)[42–44] emerging from surface-enhanced Raman spectroscopy (SERS) developed quickly with s-NSOM configuration, and achieved single molecular Raman spectroscopy and imaging[45] in 2013. Sensitive photodetectors and sophisticated optical systems lead to the successful applications of s-NSOM in various nano-spectroscopies.

In 2005, Dazzi proposed and demonstrated a photodetector-free method of performing IR subwavelength imaging [46]. This method is termed as "AFM-IR" (or Photo-Thermal Induced Resonance, PTIR), as it detects the opto-mechanical response of a contact-mode AFM cantilever induced directly by sample photothermal expansion upon excitation of IR pulses. Later, the detection sensitivity is enhanced significantly by taking advantage of the cantilever mechanical resonance and tip-enhancement effects by our group, known as the Resonantly-Enhanced IR Nanospectroscopy (REINS)[40,41], which will be presented in this dissertation. AFM-IR has outstanding performances in IR nano-spectroscopy and nano-imaging in characterizing thin polymer layers[9,40], self-assembled monolayers[41], biological samples[47,48] and plasmonic nano-structures[49,50]. We implemented the REINS system so that it works in both ambient and aqueous environment with tip and sample submerged under water[10]. The mechanism of photothermal expansion detection also led to the development of Photo-induce Force Microscopy (PiFM)[51] and Peak Force Infrared Microscopy (PFIR)[52], which measure the sample photothermal expansion with the AFM probe operating in tapping mode and achieved ~10nm spatial resolution[51,52].

Furthermore, the fast developing QCL sources in Terahertz range and IR frequency comb generation has urged people in implementing room-temperature, fast and robust IR

nano-spectroscopies without complex optical systems and bulky cryogenic-cooled detectors. The idea of using the semiconductor laser source itself as the coherent detector has attracted much attention[53–61]. In 2016, Dean demonstrated Terahertz s-NSOM based the QCL self-mixing detection principle[58] with ~1 μm spatial resolution. And Liewald has improved the resolution of the technique to 60~70 nm[60]. The implementation of mid-IR QCL self-mixing detection will be discussed in this paper.

1.3 DISSERTATION OVERVIEW

In Chapter 2, the basic operation principle of AFM-IR, including the photoexpansion force estimation and cantilever oscillation modes will be introduced. The relationship between the cantilever deflection and sample photoexpansion will be derived according to the DMT model.

Chapter 3 reported the first AFM-IR nano-spectroscopy and nano-imaging with monolayer molecule sensitivity on ~2-nm-thick self-assembled monolayers (SAMs) on atomic flat gold substrate. Only ~300 molecules contribute to the photoexpansion signal.

Chapter 4 demonstrates AFM-IR in bulk liquid cell. IR nano-spectra are obtained on 20-nm-thick polymer patterns immersed in deuterated water (D_2O). A resolution of 25 nm is achieved on 50-nm-thick patterns. Nano-spectra are also obtained on thicker films in H_2O.

Chapter 5 demonstrates AFM-IR with SAM functionalized probes. The method could potentially be applied for nano-sensing via inter-molecular chemical interactions.

Chapter 6 discusses the mechanism and experimental results of mid-IR s-NSOM detection with self-mixing effects in quantum cascade lasers. Preliminary estimation of self-mixing frequency comb operation are also calculated.

Chapter 7 gives the conclusion and outlook of the techniques presented in this dissertation.

Chapter 2 AFM Basics for photoexpansion force detection[1]

2.1 THE WORKING PRINCIPLE OF AFM-IR

In a typical AFM-IR experimental setup as shown in Figure 2.1a, an AFM probe is placed in contact with the sample. The AFM aligning laser is deflected at the head of the probe cantilever, and directed into a 4-quadrant position sensitive photodetector (PSPD) which converts the incident laser power into voltage signal. From the signal difference between the upper and lower quadrants, one could obtain the deflection distance of the cantilever. We focus the laser pulses from an IR source to the apex of the AFM tip. Upon optical absorption of the photon energy, molecules transit into an excited vibrational state. In a very short time (~10 ps[62]), the excited vibrational mode quickly dissipates into molecular vibrational modes of lower energies as well as to vibrational and kinetic modes of the surrounding molecules and substrate. Because of the anharmonicity of molecular vibrations, the effective molecular volume increases (on a macroscopic scale this leads to thermal expansion, see Figure 2.1b), which results in repulsive force acting on the AFM tip. This force leads to a small cantilever deflection and subsequent oscillation, which may be detected by the PSPD.

[1] The work presented in this chapter has been published in:
Jin, M., Lu, F. & Belkin, M. A. High sensitivity infrared vibrational nanospectroscopy in water. *Light Sci. Appl.* (2017)
Mingzhou Jin conducted the experiments and data analysis. The manuscripted is drafted by Mingzhou Jin and Dr. Mikhail A. Belkin.

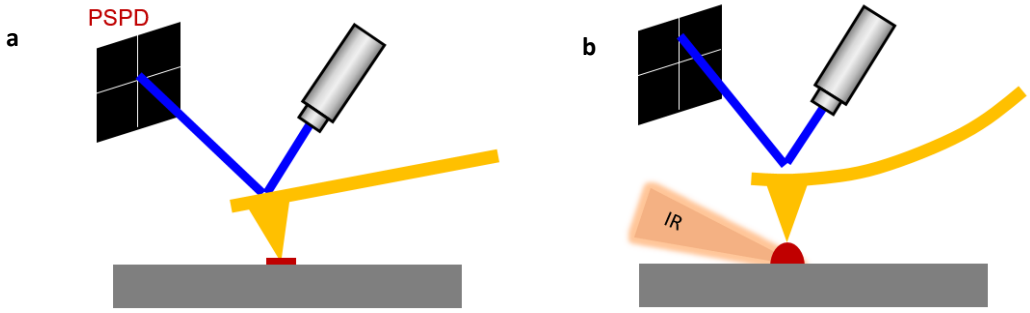

Figure 2.1: **a,** AFM cantilever deflection under IR illumination. a, AFM probe in contact with sample. **b,** Sample's thermal expansion upon IR laser excitation. The expansion force causes cantilever deflection and results in signal change on PSPD.

In the first order approximation, the force on the AFM tip is linearly proportional to the absorbed optical energy. The dependence of AFM cantilever deflection Δz on the excitation laser wavelength λ can be summarized as:

$$\Delta z \propto \alpha(\lambda) \cdot I(\lambda) \tag{2.1}$$

The AFM cantilever deflection Δz is linearly proportional to the sample's expansion distance, which is also proportional to the product of the sample absorption coefficient α and incident light intensity $I(\lambda)$. Therefore by plotting the cantilever deflection signal as a function of the incident laser wavelength, we obtain curves indicating the wavelength dependence of the sample's absorption coefficient. We call these curves 'photoexpansion spectra' because the spectral features are produced by forces due to molecular expansion under the AFM tip.

2.2 PHOTOEXPANSION FORCE

The force interaction between the AFM tip and the sample can be visualized with the AFM force-distance curve plotted in black in Figure 3a, where the *x* axis represents the spacing between tip and sample and *y* axis stands for the tip-sample force (repulsive force for positive force values and attractive force for negative force values). In static state, the tip pressed onto the sample surface at a force setpoint of F_0. For contact mode AFM, the initial indentation depth of the AFM tip is determined by the force setpoint F_0, usually on the level of tens of *nN*s. Upon the arrival of a short pulse, the sample expansion happens in ~10ps time, much faster than the AFM cantilever response time (~μs level). This would cause an instant decrease of the tip-sample distance by its expansion distance Δd, resulting in a shifted force-distance curve, as the red curve in Figure 2.2a. Consequently, an additional force ΔF is exerted onto the tip. We call this additional force ΔF the "photoexpansion force", as it is induced by the fast sample photoexpansion. The tip-sample force can further be analytically interpreted by contact mechanical models. The Derjaguin-Muller-Toporov (DMT) model of elastic contact describes the adhesive contact between a rigid sphere and elastic surfac[63] (Figure 2.2b) and is widely used to model AFM tip-sample interactions[64].

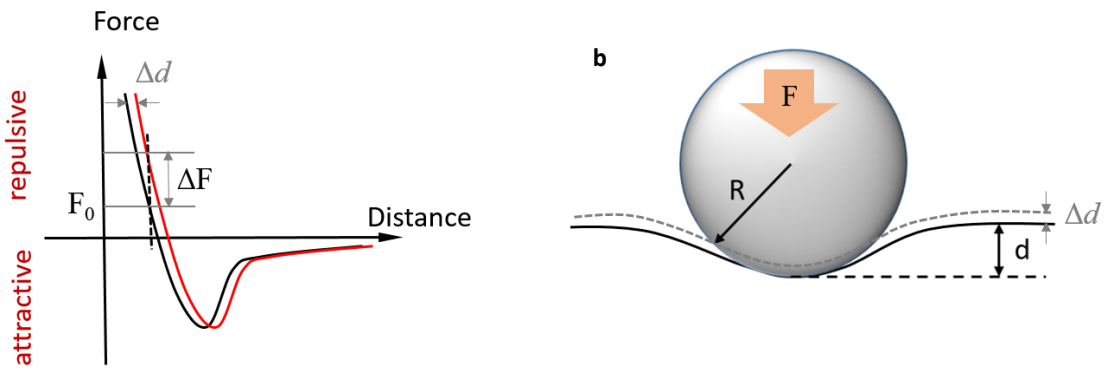

Figure 2.2: DMT model. **a,** Force-distance curve of AFM tip-sample interaction; **b,** Schematic drawing of DMT contact model.

In DMT model, the AFM tip is modeled as a sphere. The tip force F is related with the indentation depth d by:

$$F = \frac{4}{3} E^* R^{1/2} d^{3/2} - F_p \tag{2.2}$$

where E^* is the reduced Young's modulus of the sample (~5GPa), R represents the radius of the sphere (~25nm), and F_p stands for the pull-off force due to tip-sample adhesion. For a typical 100-nm-thick polymer thin film layer, the linear thermal expansion coefficient for polymer films is on the order of $10^{-4}/K$[61], which means the total sample expansion distance Δd would be 0.1 nm with temperature increase of 10K ($\Delta d << d$). By first principle approximation, the photoexpansion force ΔF can be obtained by taking the first derivative of Equation (2.2):

$$\Delta F \approx 2E^* R^{1/2} d^{1/2} \Delta d \tag{2.3}$$

2.3 CANTILEVER MECHANICS

A rectangular beam with one end fixed and the other coupled to surface, can be viewed as a damped harmonic oscillator. Therefore, the cantilever oscillation can always be decomposed into a Fourier series of multiple resonant modes. The theory of beam vibration mechanics has been extensively studied by U. Rabe *et al* [65]. Considering an elastic cantilever (length *L*, width *W*, thickness *t*) with one end fixed, the cantilever deflection $z_n(x)$ of the *n*-th flexural resonant mode can be expressed as:

$$z_n(x) = z_a[(\cos\kappa_n x - \cosh\kappa_n x) - \frac{\cos\kappa_n L + \cosh\kappa_n L}{\sin\kappa_n L + \sinh\kappa_n L}(\sin\kappa_n x - \sinh\kappa_n x)] \quad (2.2)$$

where z_a represents the vibrational amplitude and *x* is the position on the cantilever ($0 \le x \le L$, $x = 0$ is the fixed end). Here κ_n are the wavenumbers solved from the following characteristic function:

$$\sinh\kappa_n \cos\kappa_n - \sin\kappa_n \cosh\kappa_n = \frac{{\kappa_n}^3 k_c}{3k^*}(1 + \cos\kappa_n \cosh\kappa_n) \quad (2.3)$$

The spring constant of the cantilever is expressed as k_c, which is ~0.2N/m for soft contact mode cantilevers. k^* is the tip-sample contact stiffness, usually 30~1000N/m.

Consequently, the resonant frequencies f_n can also be derived from κ_n as:

$$f_n = \frac{{\kappa_n}^2}{2\pi L^2}\sqrt{\frac{EI}{\rho W t}} \quad (2.4)$$

In Equation (2.4), *E* refers to the Young's modulus of the cantilever material (usually silicon), *I* represents the area moment of inertia ($I = Wt^3/12$) and ρ stands for the cantilever material density. For a typical contact mode AFM cantilever in our setup, $W =$

$40\sim50\mu m$ and $t = 2\mu m$. The cantilever material is gold coated silicon. As the gold coating thickness is ~70*nm*, the Young's modulus *E* and density ρ is considered the same as silicon.

Typical mode shapes for a rectangular beam are plotted in Figure 2.3. Experimentally, the cantilever deflection amplitude is characterized by the AFM built-in PSPD. An aligning laser shines near the end of the AFM cantilever ($x \approx L$) and is reflected towards the PSPD. For small deflections, the PSPD signal is proportional to the cantilever slope at the end of a cantilever, which can be regarded as $z_n'(L)$, i.e. the first derivative of $z_n(x)$. In traditional contact mode AFM for topographical scanning, the cantilever deflection is operated in the 0th mode as depicted in Figure 2.3a. The factor between the PSPD signal and cantilever deflection distance $z_0(L)$ is measured as the optical sensitivity S_0:

$$S_0 = \frac{V_{PSPD}}{z_0(L)} \tag{2.5}$$

However, when higher order cantilever resonant modes are excited, the PSPD optical sensitivity at resonant frequency needs to be calibrated for different modes according to their mode shapes. From Equation(2.2), one can observe that for one cantilever, the ratio R_n:

$$R_n = \left| \frac{z_n(L)}{z_n'(L)} \right| \tag{2.6}$$

is independent of the vibrational amplitude z_a, and is only determined by κ_n, which can be calculated from k_c and k^*.

As a result, the calibrated optical sensitivity for the *n*th mode can be deduct from the measured S_0 as follows:

$$S_n = S_0 \cdot \frac{R_0}{R_n} \tag{2.7}$$

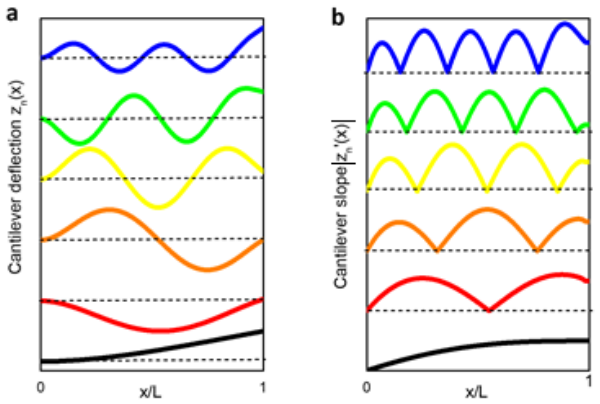

Figure 2.3: Side view of cantilever flexural mode shapes. The cantilever static deflection mode is denoted as the 0^{th} mode and plotted in black in the figure. The 1^{st} – 5^{th} surface coupled flexural modes are in rainbow colors stacked from bottom to top. **a,** Cantilever deflection amplitude as a function of position on cantilever. Dashed line represents the zero deflection position for each mode. **b,** Absolute value of cantilever slope as a function of position. Dashed line stands for zero slope for each mode.

Chapter 3 Tip-enhanced resonant AFM-IR on monolayer molecules[2]

Since the first demonstration of AFM-IR in 2005[1], there have been various applications of AFM-IR on thin polymer films and plasmonic structures[9,40,49,66,67]. However, only relative thick samples (> 50 nm) produces detectable cantilever deflections[9,40,67], and sometimes the high light power may cause thermal damage in the samples. Besides, the spatial resolution is limited by thermal diffusion length in samples and substrates, ~ 100 nm. In this chapter, we show that the sensitivity of AFM-IR (mid-infrared photo-expansion nanospectroscopy) may be improved by several orders of magnitude and that the nanoscale images can be taken with a spatial resolution effectively limited only by the AFM tip apex size.

3.1 EXPERIMENT

3.1.1 AFM-IR setup

The experimental setup is illustrated in Figure 3.1a. The AFM tip is illuminated IR light polarized along the tip shaft from a tunable QCL (range 1130cm^{-1}-1380cm^{-1}). The IR pulses incident from the side, at 75° angle relative to the surface normal. Upon the arrival of an IR pulse, the molecules that absorb the photon energy are excited to an upper vibrational states, which quickly dissipates into lower energy vibrational and kinetic

[2] The work presented in this chapter has been published in:
Lu, F., Jin, M. & Belkin, M. a. Tip-enhanced infrared nanospectroscopy via molecular expansion force detection. *Nat. Photonics* **8,** 307–312 (2014)
Mingzhou Jin and Dr. Feng Lu conducted the experiments, numerical simulations and data analysis. The manuscripted is drafted by all three authors.

modes. This leads to a fast thermal expansion of the sample below the tip apex, and cause a small cantilever deflection and subsequent oscillation. The deflection can be detected by the AFM position-sensitive photodetector (PSPD) and amplified by the lock-in amplifier (Figure 3.1a). The dependence of the AFM cantilever deflection Δz on the excitation laser wavelength λ is then expected to follow the molecular absorption spectra. Based on Equation (2.1), the sample absorption α is directly proportional to the cantilever deflection signal normalized to excitation light intensity:

$$\frac{\Delta z}{I(\lambda)} \propto \alpha(\lambda) \tag{3.1}$$

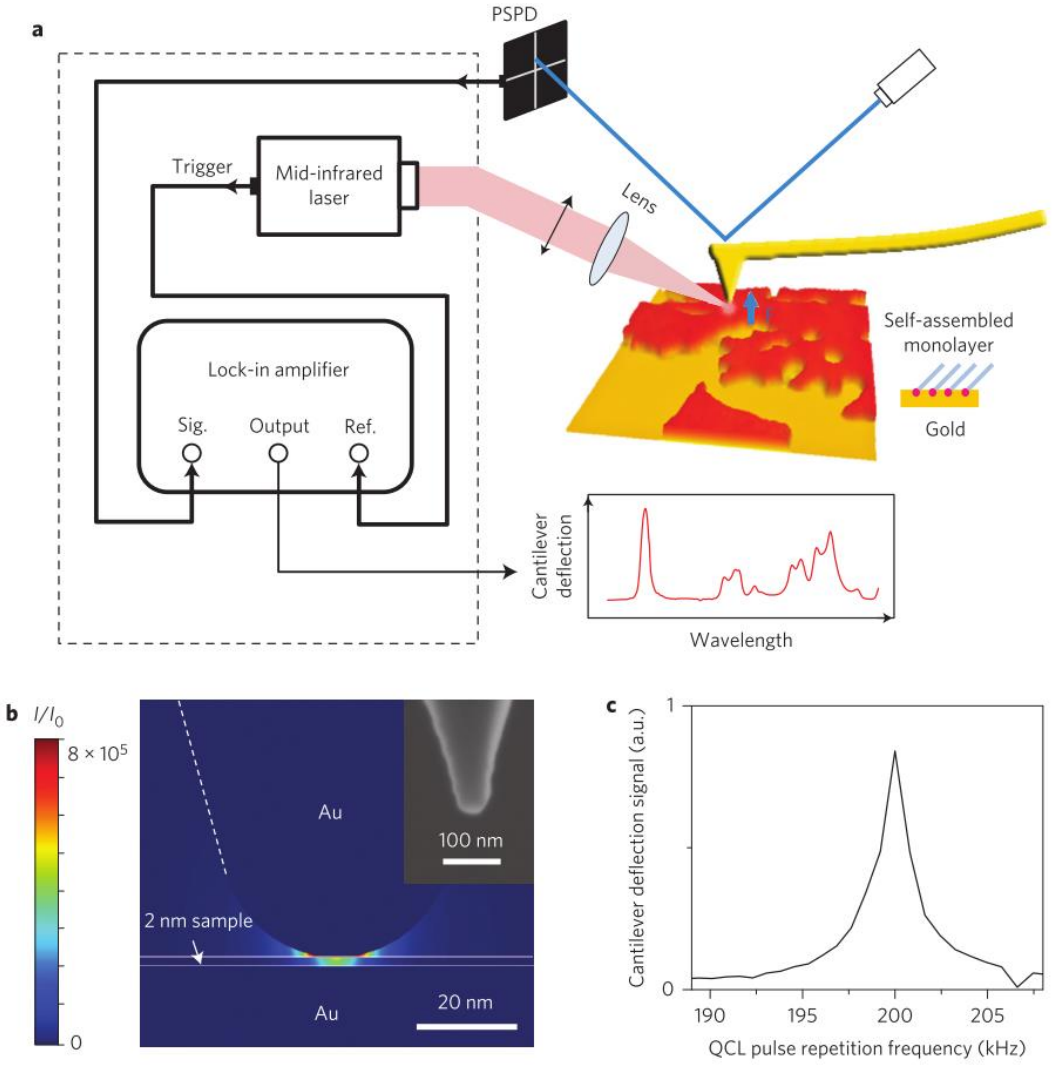

Figure 3.1: **a**, Schematic of the experimental set-up. **b,** 3-D simulation of the tip-enhancement of the light intensity (I/I_0) distribution for a 2-nm-thick molecular monolayer on gold. The mid-infrared light is incident at 75° to the surface normal. The AFM tip was modelled to have a radius of curvature of 25 nm and a half-cone angle of 17°, similar to the actual geometry seen in the scanning electron micrograph (inset). **c,** Experimental dependence of the lock-in output on the repetition frequency of QCL pulses. The data show a resonant peak at the cantilever second bending mode frequency in contact with the sample. The Q-factor is estimated from the peak linewidth to be 93.

To detect the small amount of force produced by the expansion of a few molecules below the AFM tip, we first take advantage of mechanical resonant enhancement of the cantilever deflection amplitude. This is achieved by tuning the repetition frequency of laser pulses to match a resonant frequency of one of the bending modes of the cantilever. We use a QCL as the light source, as they are electrically-pumped semiconductor lasers and their repetition frequency can be easily controlled by electric current pulses[40,68]. The cantilever deflection amplitude is amplified by the quality factor (Q factor) of a particular mode, which is ~100 for the commercially available silicon cantilevers in our setup. Therefore, the expansion relation described in Equation (2.1) can further be modified as: $\Delta z \propto \alpha(\lambda) \cdot I(\lambda) \cdot Q$.

In the experiment, we search the cantilever resonance by sweeping the laser repetition frequency and finding the frequency with the maximum cantilever deflection amplitude. In most cases, the laser repetition frequency is maintained to match the cantilever 2nd bending mode, ~200 kHz, as shown in Figure 3.1c.

However, mechanical resonance enhancement alone is not sufficient to produce monolayer sensitivity in our experiments, as shown in the previous study.[40] To achieve sub-monolayer sensitivity we also exploit tip enhancement effect in the nano-gap between the gold-coated AFM tip and the gold-coated substrate. Figure 3.1b shows the simulation of field intensity enhancement for a gold tip on a monolayer sample. For a 2-nm-thick sample representative of a typical monolayer thickness[69], the enhancement factor is calculated to be as high as 2×10^5 (Figure 3.1b). Local field intensity enhancement effectively increases the mid-

infrared absorption cross-section of molecules under the AFM tip by over five orders of magnitude and also improves the spatial resolution of our microscopy, which is now determined only by the tip apex radius.

3.1.2 Preparation of template stripped gold (TSG)

To obtain AFM images of distinct 2-nm-thick monolayer islands, the surface roughness of the gold substrate has to be smaller than 0.5 nm. One way to obtain atomically flat gold surface is using template stripped method as shown in Figure 3.2. The fabrication methods is based on the method proposed by M. Hegner *et al*[70]. The 50×75 μm mica were freshly cleaved and immediately mounted inside the chamber of an electron-beam evaporation system. 40-nm-thick gold layer was deposited on the freshly cleaved side of the mica sheet. The gold–mica sheets were then annealed in an oven for 2 h at 300°C in a nitrogen environment. The sheets were cut into smaller pieces (15×15 mm), glued onto silicon pieces with the gold surface by EPO-TEK 377 (Epoxy Technology) and cured on a hot plate at 150°C for 1 h. We then carefully peeled the mica off to expose the atomically flat gold surface. The conductivity was checked with an ohm-meter. The root-mean-square roughness of the gold surface was measured to be ~3Å for an area of 5×2.5 μm by a tapping mode AFM.

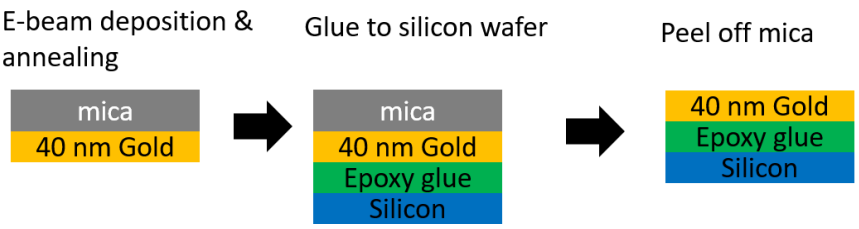

Figure 3.2: Fabrication procedure of TSG**.** 40-nm-thick gold is deposited on freshly cleaved mica sheets and annealed under 300°C for 1 hr. Then the gold side is glued to a silicon wafer using epoxy glue. After the glue is hardened, we peel the mica off by hand and expose the atomically flat gold surface.

For demonstration of high spatial resolution, poly(ethylene glycol) methyl ether thiol (PEG, $HS(CH_2)_2(OCH_2CH_2)_{21}OCH3$, 1,000 Da) SAM are also fabricated on TSG. PEG has similar absorption peaks as EG6OH but longer -(OCH_2CH_2)- chain, which results in ~2 nm thick SAM islands on TSG (shown in Figure 3.6a).

3.1.3 Preparation of self-assembled monolayers

For experimental demonstration of photoexpansion spectra, self-assembled monolayers (SAMs) were prepared on template-stripped gold (TSG) substrates. Two SAMs were tested: one made of relatively large hydroxyl-terminated hexa (ethylene glycol) undecanethiol molecules (EG6OH, molecular formula $HS(CH_2)_{11}(OCH_2CH_2)_6OH$) and one made of small 4-nitrothiophenol molecules (NTP, molecular formula $HSC_6H_4NO_2$,). The molecular structure is shown in the inset of Figure 3.5a and 3.5b. Thiolate SAMs have high affinity to the surfaces of noble metals like gold and silver[69]. We prepared SAM in ethanol solution, with ~ 1 mM concentration. And we immerse a piece of TSG sample in the solution for 24 hrs, which will allow the SAM to

form a densely-packed uniform SAM layer on the gold surface. And then we take out the TSG from the solution, rinse the sample with copious amount of ethanol and dry it under nitrogen flow. In order to measure the thicknesses of the SAMs, we cover half of the SAM sample with a silicon wafer, and exposed it to oxygen plasma in reactive ion etching. The SAM covered by the wafer will be protected, while the rest of the SAM are removed. An AFM scan is taken near the edge of the EG6-OH SAM layer in Figure 3.3a. We selected a small red box across the boundary of the SAM layer and plotted the average height along the section in Figure 3.3b, where the height of the SAM is measured as ~1.5 *nm*. The thickness of the NTP monolayer was below the topographic detection limit of our set-up and was estimated to smaller than 1 nm. We also characterized SAM samples of larger PEG molecules in Figure 3.3c. The inset shows a line scan along the blue line in Figure 3.3c. The average height of PEG SAM islands is ~2.5 *nm*.

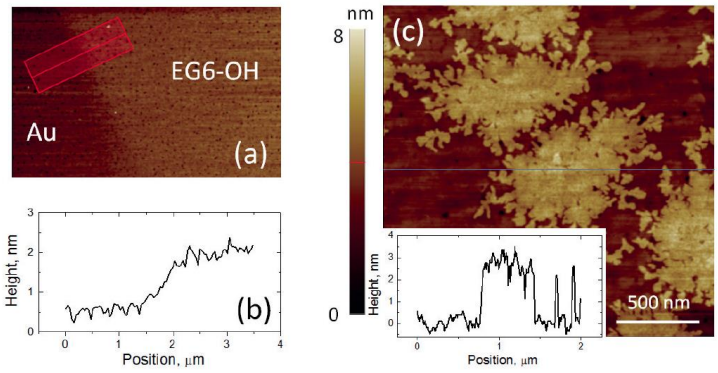

Figure 3.3: AFM topography of self-assembled monolayers. **a**, EG6-OH SAM layer; b, PEG SAM islands. **b**, Averaged line scan across the EG6-OH SAM boundary in the red box in **a**; **c**, PEG SAM layer; Inset: sample height along the blue line.

3.1.4 Spectra normalization

Photoexpansion spectra are normalized by the cantilever deflection signal taken on a clean TSG substrate (shown in Figure 3.4 in red dash), which originates from the residual broadband absorption of IR light in the AFM tip and substrate. Figure 3.4 shows a good agreement between the photoexpansion spectra on TSG and laser power spectrum $I(\lambda)$ measured with a mercury cadmium telluride (MCT) detector. Thus, the normalized photoexpansion signal would display the sample's IR absorption spectra.

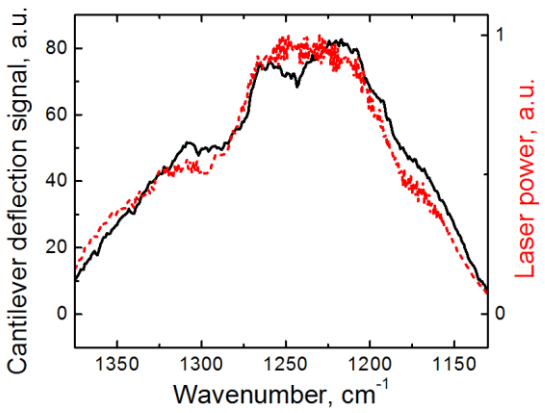

Figure 3.4: Comparison of the photoexpansion spectrum on TSG (black) and laser power spectrum obtained with an MCT detector (red).

3.2 RESULTS AND DISCUSSIONS

3.2.1 Photoexpansion nano-spectra and chemical imaging of SAMs

In the experiment, the laser repetition rate is maintained at the cantilever 2nd bending resonant mode as shown in Figure 3.1c. The photoexpansion spectra are plotted in Figure 3.5a, b for the two types of SAM samples. The cantilever deflection amplitude data were normalized to the QCL light intensity based on Equation (3.1). Figure 3.5 also shows reference absorption spectra measured by the mid-infrared reflection–absorption spectroscopy for the same monolayer material on gold in refs 71 and 72. The photoexpansion spectra are in excellent agreement with the absorption spectra.

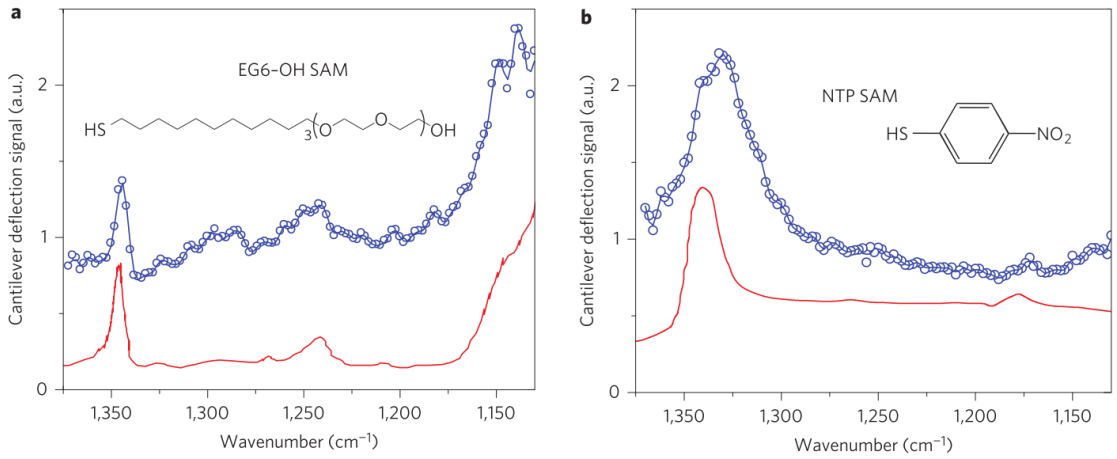

Figure 3.5: Photoexpansion spectra of self-assembled monolayers on gold. **a,** EG6OH. **b,** 4-NTP. Blue circles are measured data. Red curves are the mid-infrared reflection–absorption spectra of corresponding SAMs taken for **a** (from ref. [71]) and for **b** (from ref. [72]). Insets: molecular structure of the samples.

For EG6OH, the absorption bands centered at 1,345 cm^{-1} and 1,244 cm^{-1} correspond to CH_2 wagging and twisting modes, respectively. Due to the limited tuning range of our QCL source, only part of the stronger C-O-C stretching band (peak at 1,130 cm^{-1}) was measured. For NTP molecules, a strong peak around 1,339 cm^{-1}, corresponding to the symmetric NO_2 stretching mode, can be clearly seen. There is a weaker absorption band around 1,175–1,183 cm^{-1} corresponding to the vibration of the benzene ring. The NTP results demonstrate our ability to collect mid-infrared spectra from sub-nanometer molecules.

High spatial resolution is demonstrated with a sample made of monolayer islands of poly(ethylene glycol) methyl ether thiol (PEG) on TSG. PEG molecules have a backbone structure similar to that of EG6OH with its CH_2 wagging mode peaked at 1,342

cm^{-1}, and could form small islands on TSG substrates. The island height is ~2 nm, as confirmed by the topographic measurement in Figure 3.6a. Figure 3.6b displays a topographic line scan along the blue arrow shown in Figure 3.6a.We positioned the AFM tip at different points along the line scan (marked with squares in Figure 3.6b) and collected photoexpansion spectra at these locations. The results are shown in Figure 3.6c, where the spectra are color-coded and numbered to correspond to the measurement position markers in Figure 3.6b.We can distinguish PEG islands from bare gold by monitoring the CH_2 wagging band with a spatial resolution better than 30 nm. Figure 3.6d compares the dependence of the cantilever deflection signal along the line scan in Figure 3.6b where the laser frequency is set to the 1,342 cm^{-1} absorption line of PEG and to 1,352 cm^{-1}, away from the absorption line. As expected, the contrast between PEG and gold is only observed at 1,342 cm^{-1}. The simultaneous chemical mapping is shown in Figure 3.6e: the lock-in output is recorded as a function of tip position for the mid-infrared laser wavelength fixed at the PEG CH_2 wagging absorption band at 1,342 cm^{-1}. The bright regions are PEG molecules and dark regions are gold. The image was produced by raster scanning at a rate of 0.5 Hz with the lock-in integration time set to 3ms. The total acquisition time was 5min. And the images is in good agreement with the topography shown in Figure 3.6a.

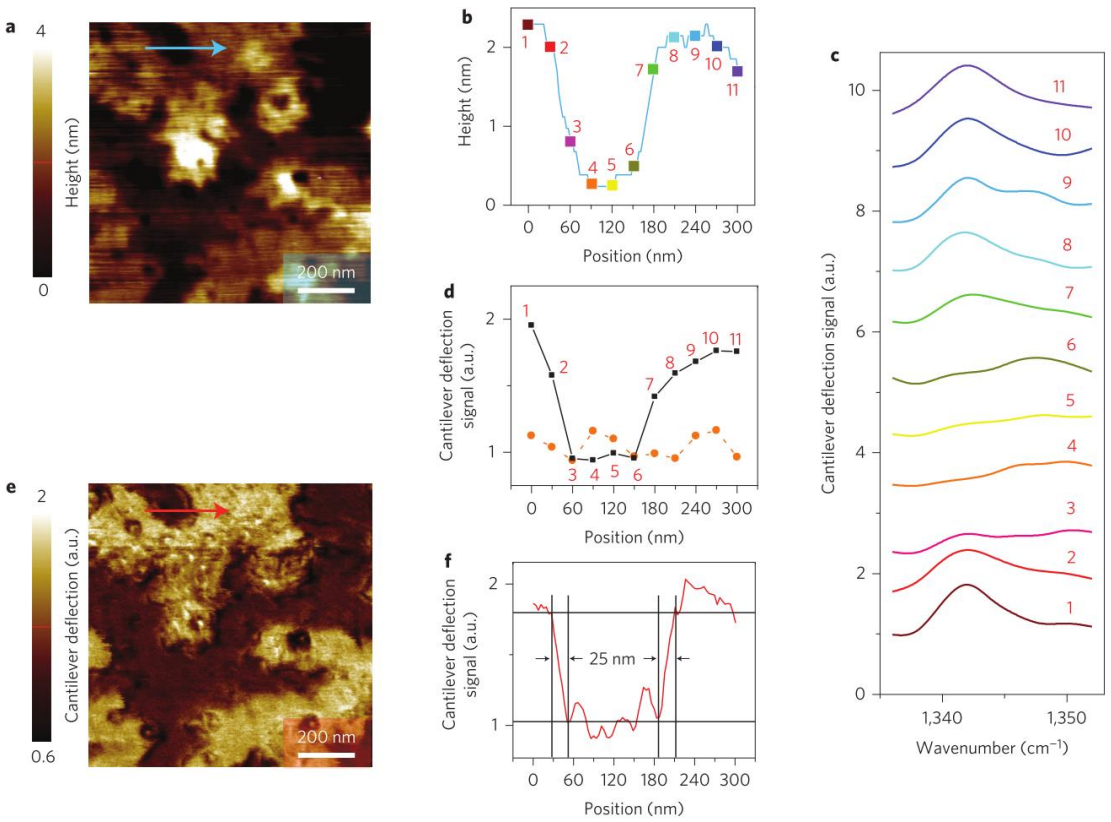

Figure 3.6: Demonstration of spatial resolution. **a**, Topography of the PEG monolayer islands acquired in contact mode. **b,** Topographic line scan along the blue arrow in a, showing the height of the monolayer islands to be ~2 nm. Square symbols mark sampling points where the AFM-IR spectra are taken. **c,** Mid-infrared photoexpansion spectra taken at the positions indicated in **b**. The curves are labelled and colored in accordance with **b**. Spectra are offset vertically. **d,** Cantilever deflection signal at different positions along the topographic scan in **b** for the laser tuned to the PEG absorption line at 1,342 cm^{-1} (black squares connected by a black solid line) and at 1,552 cm^{-1}, away from the PEG absorption line (orange circles connect by a dashed orange line). Data points are extracted from spectra in **c**. **e,** Chemical mapping of monolayer islands. The image has 256×256 pixels and was obtained simultaneously with the topographic image in **a**. **f,** Signal along the line scan shown with a red arrow in **e**. Data indicate a spatial resolution of 25 nm for the image in **e**.

3.2.2 Temperature increase simulation and cantilever deflection analysis

Figure 3.7a,b presents the simulated temperature distribution in and around the monolayer sample at the end of a 160-ns-long light pulse of intensity 1.6kW·cm^{-2} in the case where the monolayer is absorbing (Figure 3.7a) and not absorbing (Figure 3.7b). Sample heating is estimated to be below 6 K based on the results of the COMSOL simulations shown in Figure 3.7a. The low level of simulated sample heating is in agreement with the experimental observation that no signal degradation is observed for same-point measurements and that both spectral and topographic measurements are repeatable over the same sample areas.

Assuming bulk values of thermal expansion for all materials, we may estimate the tip–distance change Δd due to sample light absorption and sample expansion in both cases (Figure 3.7c). We note that Δd scales linearly with absorption in the monolayer (red line in Figure 3.7c), with a significant background level due to residual light absorption in the gold-coated substrate and the AFM tip (Figure 3.7d). Because the optical properties of gold are virtually constant in the experiment spectral range, the background is expected to be spectrally flat. The thermal parameters used in the simulation is listed in Table 3.1.

The experimental spectrum in Figure 3.5a indeed show a flat background signal with a ratio of the 1,345 cm^{-1} peak to the background level of ~1.7, which is in good agreement with the theoretical prediction of 1.5 in Figure 3.7c. The absorption-induced mechanical force on the tip, F_{abs}, is deduced using the (DMT) model of sample–tip interaction[63] as Equation (2.3): $F_{abs} \sim 2E^{*}R^{1/2}d^{1/2}\Delta d$.

Table 3.1 Thermal parameters of the materials in the simulation

Material	thickness	Refractive index	Thermal conductivity ($W \cdot m^{-1} \cdot K^{-1}$)	Heat capacity ($J \cdot kg^{-1} \cdot K^{-1}$)	Thermal expansion coefficient β (K^{-1})
SAM	2 nm	1.5 + 0.38i	0.1	1000	10^{-4}
Gold	40 nm	3.79 + 54.6i	318	129	1.42×10^{-5}
Epoxy	2 μm	1.38	0.1	1000	5×10^{-5}

The total expansion distance Δd is calculated by integrating the temperature change in the material below the tip apex and multiply by the thermal expansion coefficient β:

$$\Delta d = \int_l \beta \Delta T(l) dl \tag{3.2}$$

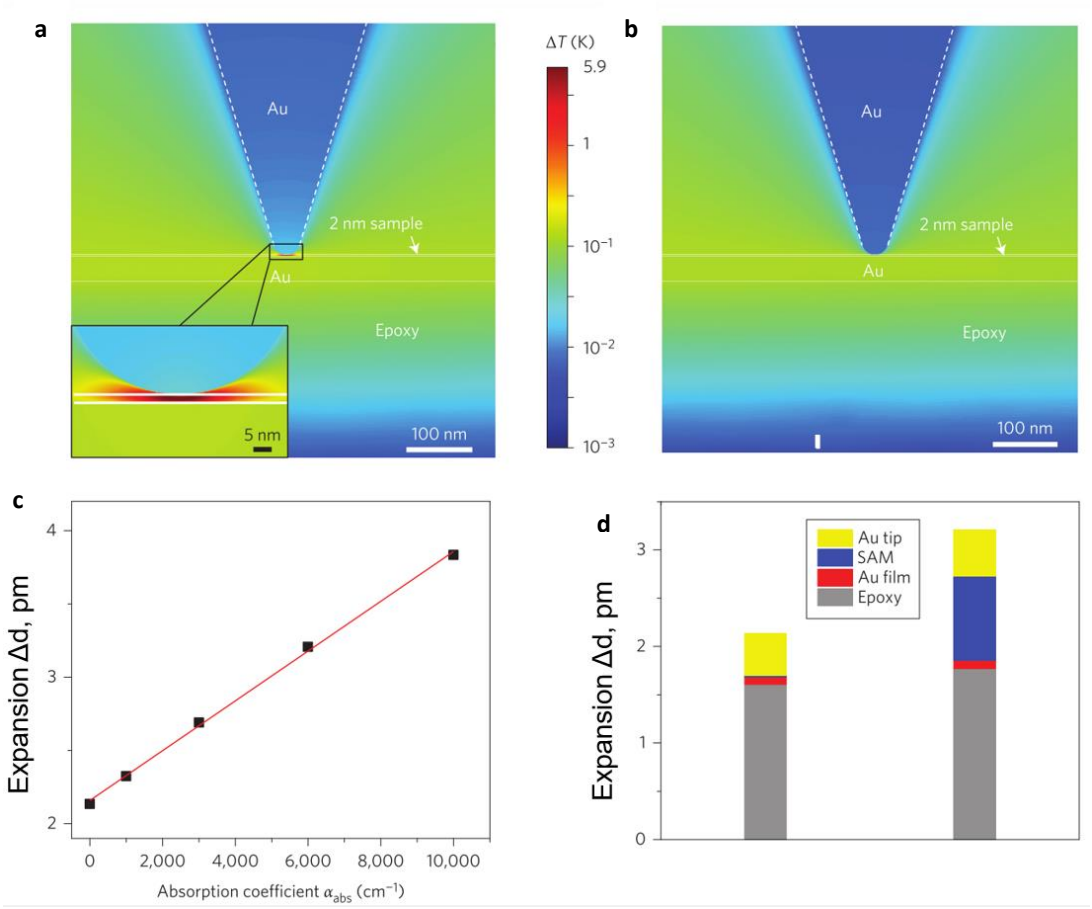

Figure 3.7: Sample heating and expansion in monolayer samples**. a,** Temperature increase distribution at the end of a 160-ns-long pulse in and around a monolayer sample below the AFM tip. The monolayer is assumed to have an absorption coefficient α_{abs}=6,000 cm^{-1}, which corresponds to absorption in PEG and EG6OH samples at1,342 cm^{-1}. **b,** Temperature increase at the end of a 160-ns-long pulse in and around a non-absorbing monolayer sample below the AFM tip. **c,** Dependence of tip–sample distance change Δd due to sample expansion caused by a mid-infrared pulse. **d,** Histograms showing the accumulated sample expansion from monolayer, substrate and tip for α_{abs}=0 cm^{-1} (left) and α_{abs}=6,000 cm^{-1} (right). The incident infrared pulse was assumed to have a peak power of 500mW and to be focused to a 100-µm-radius spot for the simulations, similar to the experimental situation.

Although the complex interaction between the nanoscale sample and AFM tip still requires further investigation, the DMT model can qualitatively explain some of the experimental results. Assuming $\Delta d \ll d$ where d is the initial indentation depth in the sample in contact mode, where R is the radius of the tip apex (25 nm) and E^* is the reduced elastic modulus of the sample (~5GPa). From ref. 64 we take the mechanical parameters for an alkane thiolate SAM on gold substrate that is similar to our EG6OH and PEG samples: $d \approx$ 0.7 nm for ~10 nN force set point. Therefore we obtain $F_{abs} = 2E^* R^{1/2} d^{1/2} \Delta d \approx 0.13nN$ for Δd = 3.2 pm (taken from Figure 3.7d). The value of F_{abs} may be used to estimate the expected cantilever deflection and compare it with experiment. We obtain a theoretical value of the cantilever deflection amplitude of 0.1 nm taking into account of the cantilever's mechanical resonance enhancement at the second bending mode.

The experimental cantilever deflection is deduced from the lock-in signal, which shows the amplitude of PSPD signal is 200mV. The optical sensitivity is 23mV/nm. The deflection and slope ratio R_0 and R_2 are calculated to be 326.9 μm and 8.34 μm respectively. As a result, $\Delta z = 200/23/326.9 \times 8.34 \approx 0.2nm$, close to the theoretical value.

In conclusion, we have demonstrated that mid-infrared vibrational spectra of molecular monolayers and monolayer islands could be collected under ambient conditions with high sensitivity and better than 25 nm spatial resolution by detecting the mechanical force exerted on an AFM tip by molecules excited with pulses of mid-infrared radiation.

We estimate that ~300 molecules contribute to cantilever deflection in our experiments. This number is based on the simulated intensity hot-spot diameter of ~10 nm (Figure 3.1b) and the molecular density of 4 molecules·nm^{-2}.[71] Given the signal-to-

background ratio in the spectra shown in Figure 3.2, we expect to be able to see strong absorption peaks from as few as 300 molecules below the tip. The sensitivity can potentially be increased further using sharper AFM tips that provide higher intensity enhancement, similar to that used for tip-enhanced Raman spectroscopy[6,73], and AFM cantilevers with higher Q-factors. Even at this present stage, the mid-infrared spectra reported here are of higher quality than the mid-infrared spectra produced by the state-of-the-art s-NSOM for monolayer or thin-film samples[3,37].

Chapter 4 High-sensitivity IR vibrational nanospectroscopy in water[3]

Vibrational nano-spectroscopy can reveal the chemical composition of samples on nanoscale, and several techniques have been developed to address this need. It is highly desirable to study biological and chemical samples in their native aqueous environments rather than in air. However, in aqueous environment, the performance of current vibrational nano-spectroscopies deteriorates dramatically.[26,47]

Current state-of-the-art results include IR nano-imaging of a 6-μm-diameter Melamine beads in water with ~1 μm spatial resolution using aperture NSOM[26] and an AFM-IR nanospectroscopy of ~1-μm-thick Candida albicans fungi[47] in 850–1250 cm^{-1} spectral range. IR s-NSOM imaging of samples in ultra-thin graphene covered liquid cell has also been recently demonstrated[74]. In this case, the sample was covered by an ~10-nm layer of water below a graphene sheet, and the AFM probe was operated in air. However, ultrathin graphene liquid cells are difficult to implement and are known to subject samples to very high-hydrostatic pressure (ca. 1 GPa)[74].

Here, we demonstrate that high-sensitivity infrared nanospectroscopy can be performed in bulk liquid cells, thus avoiding the complications associated with nanoscale liquid cells.[10] Our method is based on the resonantly enhanced infrared photoexpansion

---

[3] The work presented in this chapter has been published in:
Jin, M., Lu, F. & Belkin, M. A. High sensitivity infrared vibrational nanospectroscopy in water. *Light Sci. Appl.* (2017)
Mingzhou Jin conducted the experiments and data analysis. The manuscripted is drafted by Mingzhou Jin and Dr. Mikhail A. Belkin.

nanospectroscopy (REINS) technique discussed in Chapter 3. REINS detects sample absorption via a non-optical method, and unlike NSOM, it is insensitive to light scattering.[40,41]

4.1 EXPERIMENT

The schematic of our experimental setup is shown in Figure 4.1a. We illuminate the sample with a train of optical pulses from a quantum cascade laser through a germanium prism. The sample is positioned on top of the prism for evanescent illumination, and a gold-coated silicon tip is placed in contact with the sample. A cover glass slide, attached at the back of the cantilever chip holder, holds a water droplet between the glass slide and prism. In order to reduce water absorption and enhance the cantilever oscillation amplitude, we improved the field enhancement and cantilever resonance in water environment.

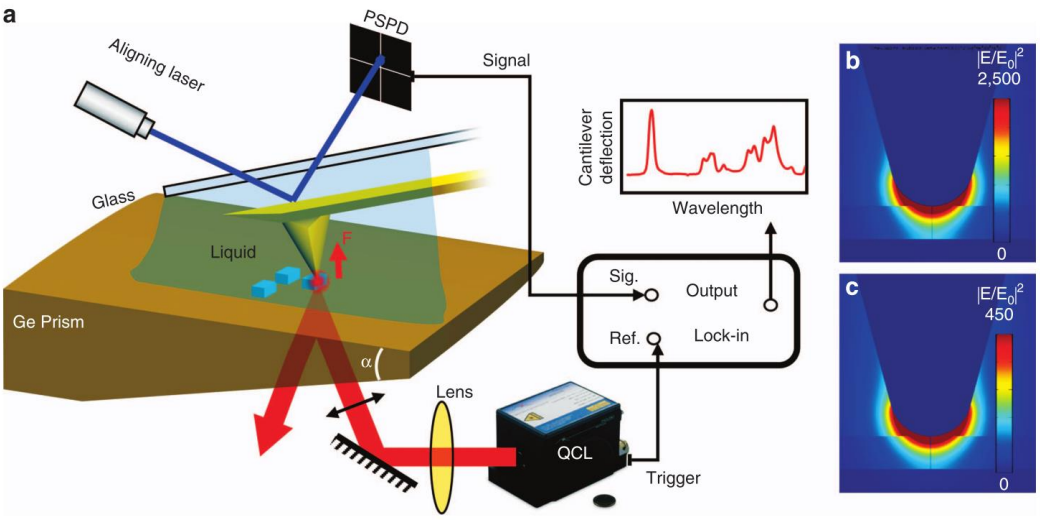

Figure 4.1: continued on the next page.

Figure 4.1: Experimental setup and tip enhancement simulations. **a,** Experimental setup for the photoexpansion nanospectroscopy in liquid. The polarization of the incident light is parallel to the incident plane. The wedge angle α is 14.5°. **b,c,** Optical field intensity enhancement below the metallized AFM in the case of a sample (PMMA) on top of a germanium prism **b** and a ZnSe prism **c**.

4.1.1 Evanescent illumination and field enhancement

In an aqueous environment, mid-infrared nanospectroscopy techniques encounter two major challenges. One is the strong mid-infrared light scattering and absorption in water, which can overwhelm the signal from the sample.

We suppress the water absorption by nanofocusing the laser light onto the sample volume immediately below the AFM tip. To achieve this, the sample is evanescently illuminated using a *p*-polarized laser light, and the optical field intensity in the sample below the AFM tip is enhanced because of a combination of the electrostatic boundary condition effect at the prism–sample interface[75] and the tip enhancement due to the metallized AFM tip[41,76].

According to the Maxwell's equations, the amplitude of the z-component of the far-field transmitted evanescent wave $|E_{z0}|$, can be expressed as a function of the incident wave amplitude $|E_0|$ and the incident angle θ:[75]

$$\left|\frac{E_{z0}}{E_0}\right| = \frac{2\cos\theta\sin\theta}{\left[\left(\frac{n_{liquid}}{n_{prism}}\right)^4 \cos^2\theta + \sin^2\theta - \left(\frac{n_{liquid}}{n_{prism}}\right)^2\right]^{1/2}} \tag{4.1}$$

If θ is set to the critical angle of the prism/liquid interface, $\left|\frac{E_{z0}}{E_0}\right|$ will reach the maximum value:

$$\left|\frac{E_{z0}}{E_0}\right|_{\max} = \left|\frac{2n_{prism}}{n_{liquid}}\right| \tag{4.2}$$

Here, n_{prism} and n_{liquid} are the refractive indices of the prism and liquid respectively. As a result, we use a prism made of germanium, which has the highest dielectric constant ($\varepsilon_r^{Ge} \approx 16$) of all the mid-infrared materials and provides the strongest field enhancement. Tip-enhancement of the evanescent optical field intensity at Ge/water interface is simulated and plotted in Figure 4.1b. The importance of a germanium prism is illustrated in Figure 4.1c, which shows the optical field intensity below the AFM tip for the case of a ZnSe prism ($\varepsilon_r^{ZnSe} \approx 5.8$), which has a significantly lower dielectric constant than germanium. Therefore, the incident angle θ is set to 19.4° for Ge/water interface.

Furthermore, Figure 4.1b shows that despite the nanofocusing, a small fraction of the liquid surrounding the tip may still be exposed to a high-intensity optical field, thus resulting in significant liquid photoexpansion. Heavy water (D_2O), compared with water (H_2O), has a much smaller absorption coefficient in the Amide I and II bands[77]. Therefore, we chose to operate in the D_2O environment.

4.1.2 Cantilever resonances in liquid

The second challenge faced by the mid-infrared nanospectroscopy techniques in water is strong mechanical damping of the cantilever oscillations. The Q-factor of the fundamental cantilever mechanical resonance can decrease from ~100 in air to only ~1 in

water[78].The resonance peak broadening makes it very challenging to operate an AFM in non-contact or tapping modes[79]. In contrast to the NSOM and photo-induced force microscopy techniques, resonantly-enhanced AFM-IR records sample spectra by operating the AFM in contact mode, thereby less sensitive to this problem.

However, liquid damping still has influence on resonantly-enhanced AFM-IR through the decrease in the Q-factor and shifting the cantilever resonance significantly to lower frequencies. To boost the signal level, we tune the rate of laser pulses to excite the higher-order cantilever flexural modes that are expected to have higher Q-factors in liquid. In liquid, the *n*th resonant frequency $f_{l,n}$ and the corresponding Q factor $Q_{l,n}$ can be approximated by the model proposed by J. Sader *et al*, in the limit of small dissipative effects.[80–83] The values of $f_{l,}$ and $Q_{l,n,}$ can be deduced from the resonant frequency in air $f_{a,n}$:

$$\frac{f_{l,n}}{f_{a,n}} = [1 + \frac{\pi \rho W}{4 \rho_c t} \Gamma_r(f_{l,n})] \tag{4.3}$$

$$Q_{l,n} = \frac{\frac{4\rho_c t}{\pi \rho W} + \Gamma_r(f_{l,n})}{\Gamma_i(f_{l,n})} \tag{4.4}$$

Here, Γ_r and Γ_i are the real and imaginary components of the hydrodynamic function $\Gamma(f)$. For the given cantilever structure and the fluid density and viscosity, Γ can be expressed as a function of cantilever resonance wavenumber κ_n (see Equation (2.2)

(2.3)),. ρ and ρ_c stands for the liquid density and cantilever density respectively. The theoretical values are calculated and listed in Table 4.1.

The experimentally measured cantilever mechanical resonances in water and their Q-factors are shown in Figure 4.2. For the cantilever flexural modes above the 4th mode, the cantilever slope varies significantly over the 40-μm aligning laser spot diameter, thus resulting in a decrease signal amplitude in the PSPD signal, which limited our setup to the 4th flexural mode with a Q-factor of 9.9.

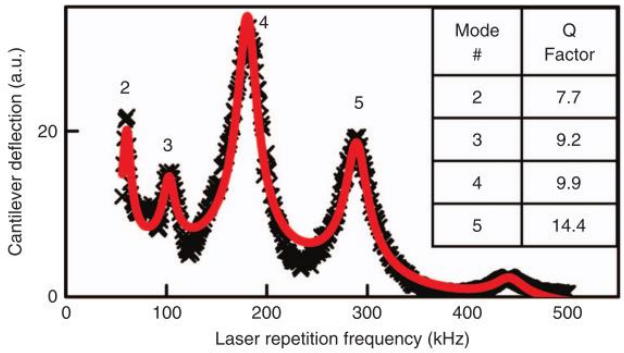

Figure 4.2: Cantilever resonant modes in water. Experimentally measured cantilever vibrational spectrum in D_2O (black crosses), fitted using five resonant modes (red curve). The Q-factors of the four modes are listed in the inset.

Table 4.1 Theoretical and Experimental resonant frequency in air and in liquid

Mode # n	Theoretical			Experimental	
	κ_n	f in water (kHz)	Q in water	f in water (kHz)	Q in water
2	6.688	58.4	7.2	59	7.7
3	9.039	108.1	9.0	103	9.2
4	11.483	175.9	11.3	180	9.9
5	14.350	276.5	13.7	288	14.4

4.2 RESULTS AND DISCUSSION

4.2.1 AFM-IR nano-spectra normalization in D_2O and H_2O

For a proof-of-concept demonstration, we fabricated nanoscale patterns of 20- and 50-nm-thick layers of Poly(methyl methacrylate) (PMMA) on top of the Ge prism.

According to the optical field simulation in Figure 4.1b, a small fraction of the liquid surrounding the tip may still be exposed to a high-intensity optical field, resulting in water absorption background. Therefore, the photoexpansion spectra of the sample were obtained by normalizing the cantilever oscillation amplitude to the laser intensity (cf. Equation (3.1)) and subtracting the D_2O background signal, as we assume that the liquid photoexpansion and the sample photoexpansion produce additive effect on the cantilever deflection amplitude. The photoexpansion background (BG) spectrum of D_2O is obtained by moving the cantilever to a position on a prism without a polymer film. Figure 13a shows

the photoexpansion spectra (after normalized to laser intensity) of the sample covered in heavy water and of the photoexpansion background spectrum of D_2O. By subtracting the D_2O BG, we obtain the spectrum of a 20-nm PMMA in D_2O as plotted in blue in Figure 4.3b. It features a sharp peak at 1730 cm^{-1}, corresponding to the C=O stretching mode of PMMA. The signal-to-noise ratio of these measurement was estimated to be ~5. Figure 4.3b also shows an infrared absorption spectrum of bulk PMMA in red line, which is in excellent agreement with the measured spectrum.

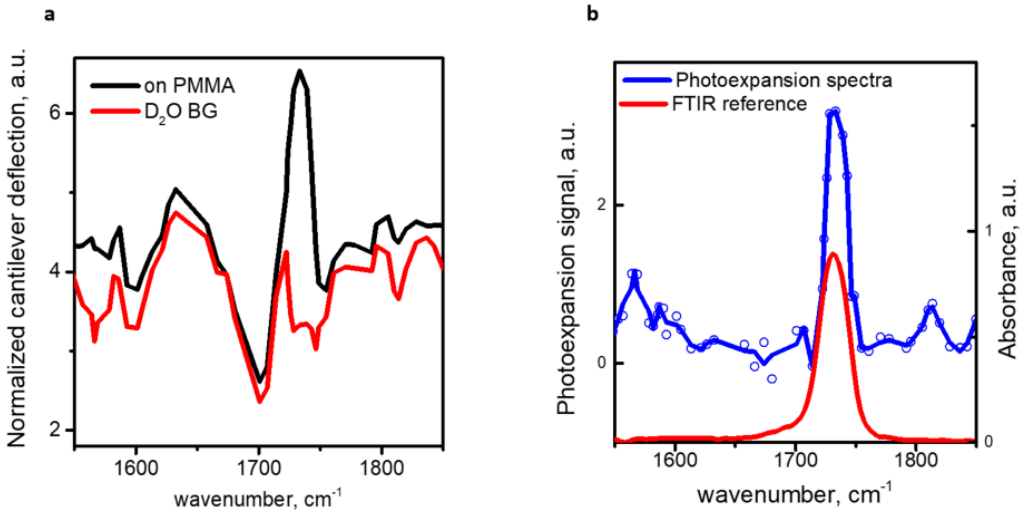

Figure 4.3: Photoexpansion spectrum of PMMA. **a,** Cantilever deflection signal normalized by the laser intensity. Black line shows the case of the AFM tip positioned on top of a 20 nm thick PMMA film in D_2O. Red line shows the case of the AFM tip positioned on top of a bare prism in D_2O. **b,** Normalized photoexpansion spectrum of a 20-nm-thick PMMA film in D_2O (blue line) vs the reference Fourier transform infrared spectroscopy (FTIR) absorption spectrum of PMMA (red line).

For comparison, photoexpansion spectroscopy were also performed in H_2O environment on 150-nm-thick PMMA film. Regular water (H_2O) has significantly higher absorption in the Amide I and II region, compared to D_2O as shown in Figure 4.4a. As a result, samples immersed in H_2O showed 5-10 times higher background signal which prevented us from obtaining high-quality nanoscale spectra from thin PMMA samples immersed in H_2O. PMMA samples over 100 nm in thickness, however, produced high quality nanoscale spectra in H_2O as shown in Figure 4.4b,c for the case of 150-nm-thick PMMA sample.

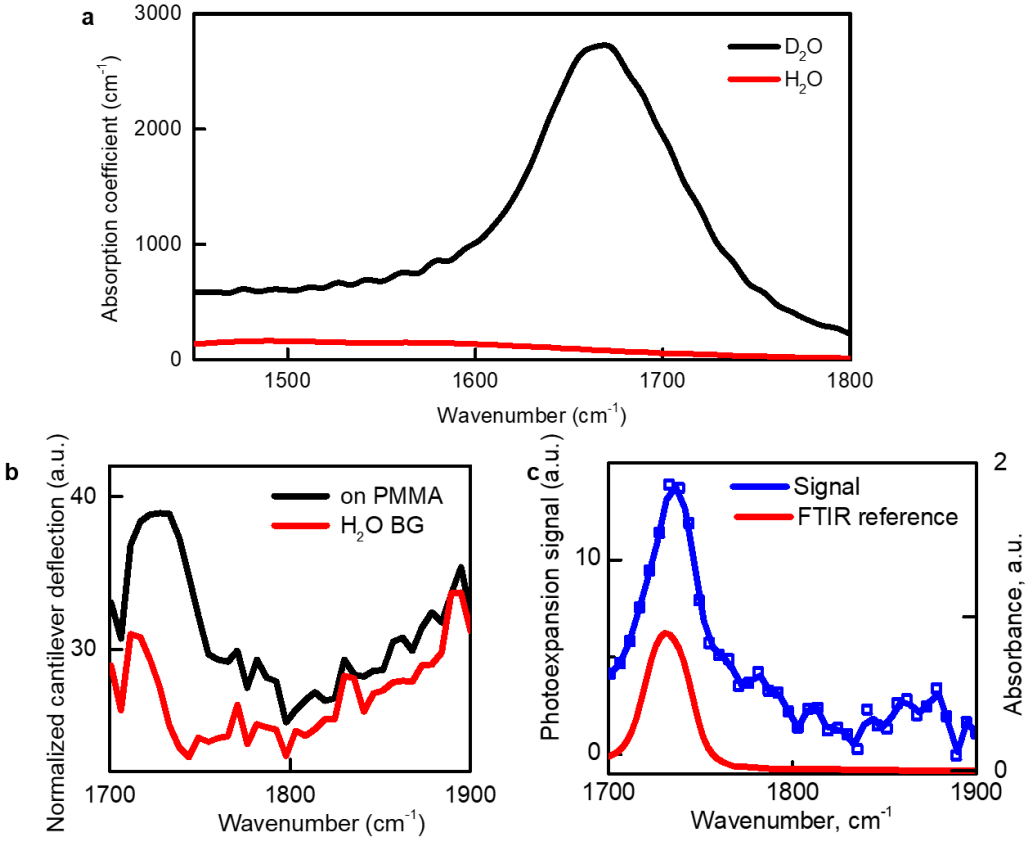

Figure 4.4: continued on the next page.

Figure 4.4: Photoexpansion spectrum of 150-nm-thick PMMA in H_2O environment. **a,** Absorption spectrum of H_2O and D_2O in the Amide I and II region. **b,** Cantilever deflection signal normalized by the laser intensity vs laser wavenumber. Black line shows the case of the AFM tip positioned on top of a 150-nm-thick PMMA film in H_2O. Red line shows the case of the AFM tip positioned on top of a bare prism in H_2O. **c,** Normalized photoexpansion spectrum of a 150-nm-thick PMMA film in H_2O in blue and the Fourier-transform infrared spectroscopy (FTIR) absorption spectrum of PMMA in red.

4.2.2 Optimization of incident angle

In order to understand the effect of incident angle on the signal quality, we measured the AFM-IR nano-spectra on 100-nm-thick PMMA film deposited on Ge prism in D_2O at different incident angles, plotted in Figure 4.5. The critical angle at germanium and water interface can be calculated by $\theta_c = \arcsin\frac{n_{D_2O}}{n_{Ge}} = 19.4°$. When incident angle is above the critical angle, light undergoes total internal reflection at the germanium/water interface, and the polymer film is illuminated via evanescent field. The carbonyl peak at 1730 cm^{-1} is obvious compared with the background signal. The closer the incident angle is to the critical angle, the larger photoexpansion signal magnitude at the absorption line is achieved. And once the incident angle becomes smaller than the critical angle, IR light will shine through the water. Consequently, the water background increases and the photoexpansion signal at the absorption peak cannot be distinguished from the background. In the experiment, the incident angle is set at ~20° for the optimized signal to background ratio.

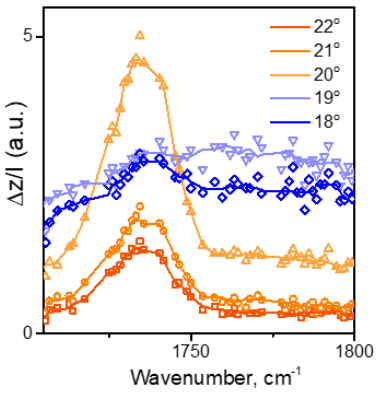

Figure 4.5: Normalized AFM-IR spectra with different incident angle measured on 100-nm-thick PMMA film in D_2O.

4.2.3 Spatially resolved IR nano-spectra in D_2O

To demonstrate the spatial resolution of our technique, we performed spectroscopy and imaging of a 50-nm-thick PMMA pattern on a germanium prism in D_2O. Figure 4.6a exhibits the AFM topography of a single 'UT' logo. We took the spectra at 30 points, at 25-nm intervals, along the arrow in Figure 4.6a. The selected spectra are shown in Figure 4.6c. The PMMA absorption peak appeared only when the tip was on top of the PMMA. To further demonstrate the nanoscale resolution of our technique, Figure 4.6d plots the photoexpansion signal strength at the laser wavenumber of 1,730 cm^{-1} (at the PMMA peak) and at 1,760 cm^{-1} (away from the PMMA peak) against the sample topography as a function of the tip position. The contrast was observed only at the PMMA absorption peak at 1,730 cm^{-1}, and the signal followed the shape of the topographical line scan.

Figure 4.6b shows the mid-infrared chemical mapping. In this case, we set our laser wavelength to the PMMA infrared absorption peak and measured the cantilever deflection

signal as a function of the tip position. The area imaged in Figure 4.6b was the same as that of the topographic image in Figure 4.6a, and a clear contrast in the PMMA patterns was observed.

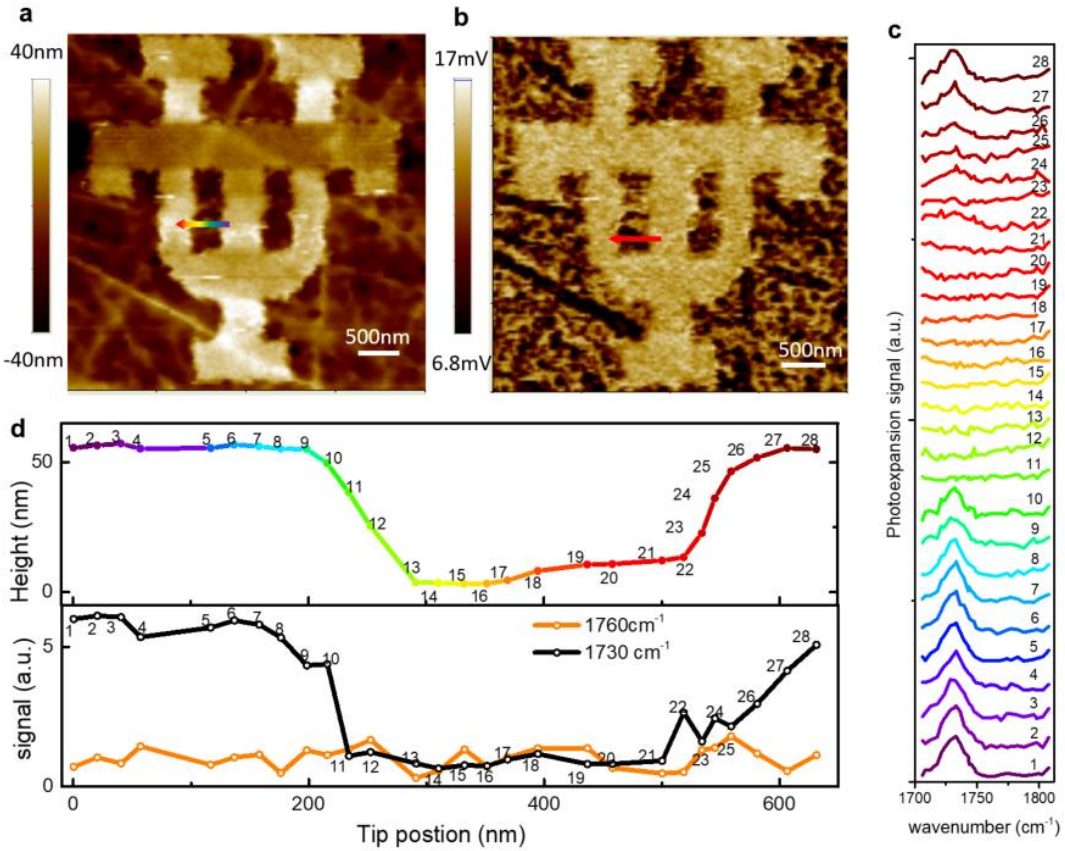

Figure 4.6: Photoexpansion spectra and chemical mapping on 50-nm-thick PMMA pattern. **a,** AFM topography of a 50-nm-thick PMMA pattern. Bright areas are the PMMA film, and dark areas are the bare germanium. **b,** Photoexpansion spectra, taken at 25-nm intervals along the arrow shown in **a**. **c,** Topography (top) and the REINS signal (bottom) at 1730 cm^{-1} (black) and 1760 cm^{-1} (orange), taken at 25-nm intervals along the scan line shown in **a**. **d,** Chemical mapping of the sample area shown in **a**.

4.2.4 Simulation and discussion

Figure 4.7a shows the simulated temperature distribution in a 20-nm PMMA sample and in the surrounding D_2O at the end of a 300-ns laser pulse of intensity 3.9kW·cm^{-2}. Our simulations showed that the sample experiences a maximum temperature increase of ΔT=2.8 K at the end of the laser pulse, which is comparable to the ΔT=5.9 K calculated for the monolayer sample on gold-coated substrates by using the REINS technique in air. Figure 4.7b shows that D_2O heating was present, owing to liquid absorption, even when the sample was non-absorbing. The heating was significantly higher in the H_2O environment, as plotted in Figure 4.7c, thus preventing us from measuring high-quality spectra from the PMMA samples in H_2O below 100 nm in thickness.

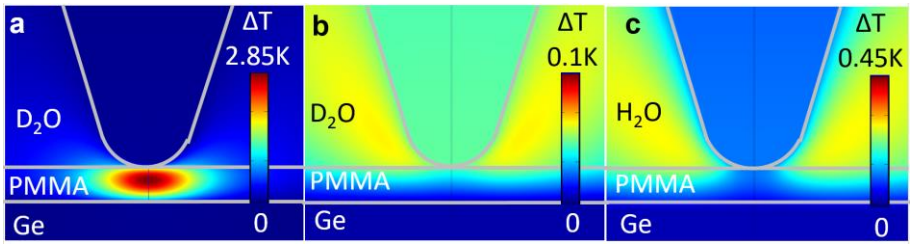

Figure 4.7: Temperature increase in the sample during the laser pulse. Simulated temperature distribution in the 20-nm-thick PMMA sample at the end of a 300-ns QCL pulse, assuming **a,** a PMMA absorption coefficient of α_{abs}=5400 cm^{-1} (corresponding to the peak PMMA absorption at 1730 cm^{-1}) at the laser wavelength and the sample being immersed in D_2O, **b,** PMMA not absorbing (α_{abs}=0) at the laser wavelength and the sample being immersed in D_2O, and **c,** PMMA not absorbing (α_{abs}=0) at the laser wavelength and the sample being immersed in H_2O.

The AFM tip displacement $z_0(L)$ (cf. Equation (2.5)) is measured by detecting the aligning laser beam deflected from the end of the cantilever onto the position sensitive photodetector.

The optical sensitivity of our setup in water is measured to be S_0 = 30.6 mV·nm^{-1}. By fitting experimental data, we obtain that $k^* = 35N \cdot m^{-1}$. Calculated values for R_0 and R_4 are 327μm and 60μm according to Equation (2.6), respectively. The maximum amplitude of the V_{PSPD} signal is measured to be 2.7 mV in the photoexpansion spectroscopy experiment on top of a 20-nm-thick PMMA sample in heavy water with the water background signal subtracted. It translates to a tip displacement of:

$$z_4(L) = \frac{V_{\mathrm{PSPD}}}{S_W} \cdot \frac{R_4}{R_0} = 16.1pm \tag{4.3}$$

The tip deflection amplitude is more than 10 times smaller than that in Chapter 3 for the measurements of the monolayer sample on a gold substrate in air[41].

In summary, we have demonstrated a technique for the high-sensitivity vibrational nanospectroscopy of chemical samples in an aqueous environment. We achieved a spatial resolution of 25 nm and obtained spectra of polymer samples as thin as 20 nm. Our work lays a foundation for the infrared nanospectroscopy of chemical and biological samples in their native liquid environments and offers the possibility of in vivo studies of biological samples using infrared nanospectroscopy.

Chapter 5 Resonant AFM-IR with Functionalized Tips

Tip functionalization has become an important technique to directly probe the interactions between molecules on few molecule level. Functionalized tips are widely applied in dip-pen nanolithography[84,85] and nano imprint lithography[86], where functional molecules are manipulated by AFM probes for nanostructure fabrication. Functionalized tips can even work as catalyst to induce highly-localized nanochemistry[87,88], and create patterns with nanoscale spatial resolution on monolayers. Apart from nanofabrication, high resolution imaging has been achieved with probes functionalized with molecules[89], nanocrystals[90] or nanotubes[91]. In 2009, atomic force microscopy (AFM) image[89] of a single pentacene molecule is demonstrated with CO functionalized probes. Moreover, chemical force microscopy (CFM) has been developed to image the sample's chemical properties. By using tips functionalized with hydrophobic or hydrophilic chemical groups, one can characterize surfaces via the intermolecular adhesion and desorption forces between the tip and the surface.[92–94]. Furthermore, if the tip and substrate is functionalized with the opposite components of a specific molecular pair, for example, biotin-avidin pair, one can perform molecular recognition in CFM.[95,96]

There is only a few molecules on the apex of a functionalized AFM tip, therefore spectroscopic studies of AFM tip coatings require techniques with close-to-single-molecule sensitivity. Presently, there are only a few techniques that can perform vibrational spectroscopy on monolayer molecules on sharp metal tips. Inelastic electron tunneling spectroscopy (IETLS)[97], is able to obtain vibrational spectra on single molecule with STM. However, the technique subjects to ultrahigh vacuum and substrate conductivity and cannot

be used for in situ spectroscopy in ambient conditions. TERS is another method to measure Raman spectra of functionalized tips[98,99]. But the plasmonic enhancement of the near-field optical field varies greatly depending on the shape of the metalized tip apex, which results in huge deviation in tip performances.[99]

Here we report infrared vibrational spectroscopy on the molecules on the functionalized AFM tip apices using resonantly enhanced infrared photoexpansion nanospectroscopy (REINS)[40,41], also known and resonantly-enhanced AFM-IR technique[1]. We estimate that fewer than 50 molecules on the AFM tip apex contributed to the observed spectra. Our results establish a new technique for chemical characterization of functionalized AFM tips and may potentially allow performing infrared vibrational spectroscopy of nanoscale reactions as well as spectroscopic monitoring of molecular conformational changes and molecular interactions on the apex of the AMF tip.

5.1 EXPERIMENT

5.1.1 AFM-IR setup

In this experiment, we use bottom-illumination and shine light through a germanium prism[10] in contact with the functionalized tip apex(shown in Figure 5.1a). High field intensity enhancement appear at the interface of the high-index prism and free space when light incident angle in germanium is approximately at the critical angle, i.e. 14.5° for Ge/air interface. As a result, transmitted field amplitude can be 8 times larger as the incident field amplitude according to Equation (4.2). The evanescent field decays

exponentially into air, with an evanescent tail extending about a few microns above the Ge/air interface.

Tip enhanced local field intensity under the tip apex is simulated with finite element method (see Figure 5.1b). We assume the AFM prove is covered with 2 nm thick uniform absorbing layer as the monolayer. In the simulation result, there is up to 10^6 enhanced optical field intensity localized below the tip apex. The maximum intensity inside the concentrated field can be more than 10^6 times higher than the incident field, and radius of the hotspot is about 5 nm. Figure 5.1c shows the field enhancement at the same tip apex when the tip is lifted 100 nm above the prism with the same illumination condition. The maximum field intensity drops more than100 times compared to Figure 5.1b.

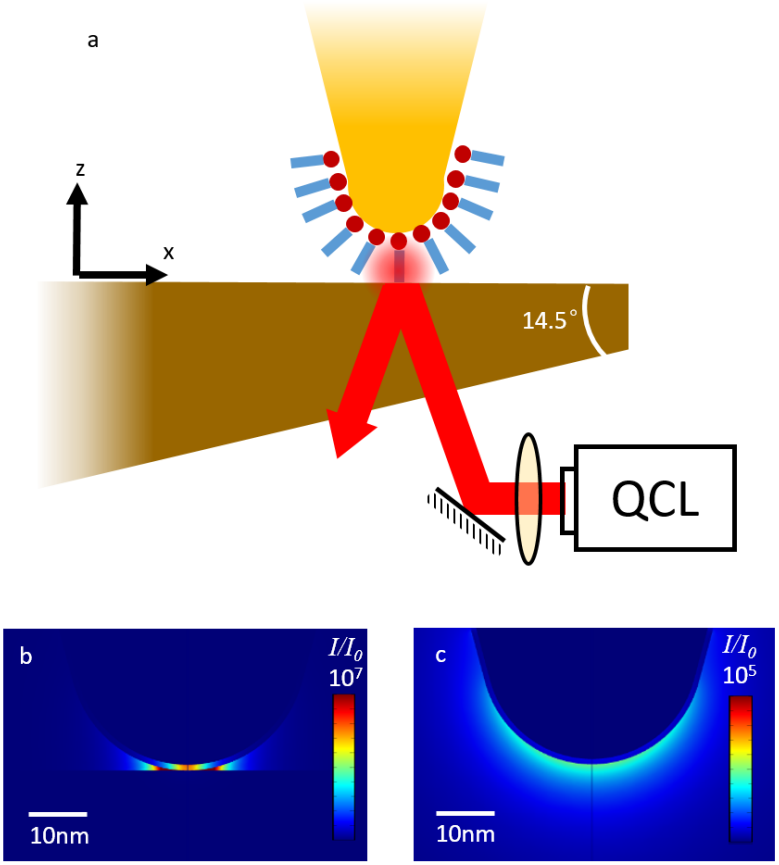

Figure 5.1: **a,** Experimental setup; **b,** Simulation of light field intensity enhancement surrounding the tip apex when the functionalized tip is in contact with prism, and **c,** lifted to 100 nm above the prism.

5.1.2 Preparation of functionalized tips

For experimental demonstration, the tips are functionalized with self-assembled thiolate molecules[69]. We choose 4-Nitrothiophenol (NTP) and hydroxyl-terminated hexa(ethylene glycol) (EG6OH) as the SAM layer and prepare the probes respectively. Newly purchased AFM probes (ContGB-G from BudgetSensors) are immersed in acetone for 3hrs to remove organic contaminants. After that, the probes are incubated in 1mM SAM

(NTP or EG6OH) ethanol solutions for 12 hrs, and a densely-packed monolayer will form uniformly on the gold surface. Then the probes are rinsed with copious amount of ethanol and dried under gentle nitrogen flow.

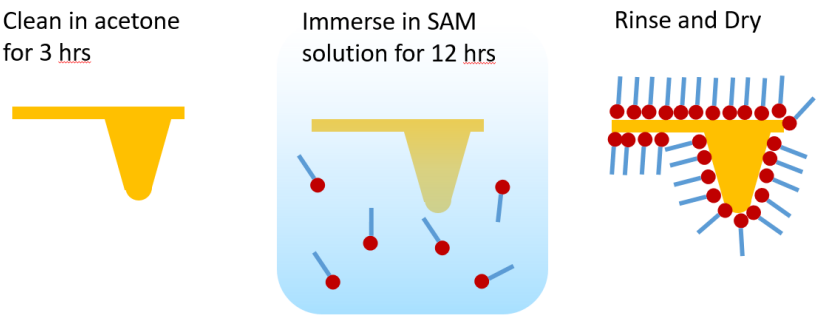

Figure 5.2: Fabrication procedure for SAM functionalized AFM tips.

The removal process of the functional molecules is performed by placing the functionalized probes under low-power oxygen plasma for 20 min.

5.1.3 Spectra normalization

The normalized spectrum is obtained by dividing the photoexpansion signal of the functionalized tip by its own background spectrum, which is taken immediately after the new tip is cleaned in acetone. The background signal purely comes from the interaction between the laser and the gold-coated probe itself, regardless of any functionalized molecules, and follows the shape of laser power spectrum $I(\lambda)$ as shown in Figure 5.3.

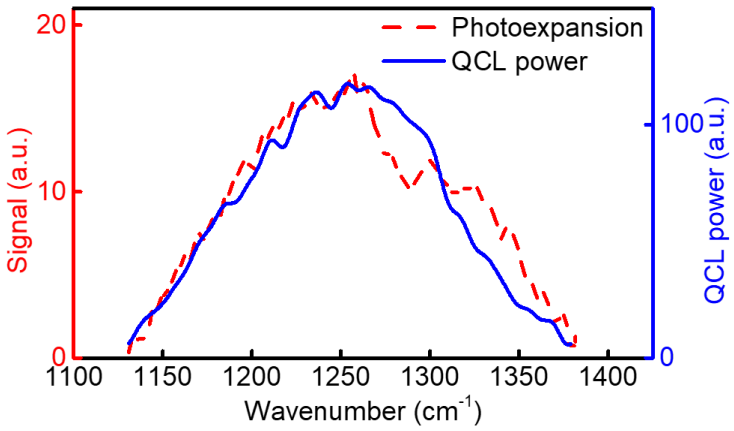

Figure 5.3: Comparison of photoexpansion nano-spectrum of a clean probe on Ge prism (red) and laser power spectrum (blue).

5.2 RESULTS AND DISCUSSION

The probes are mounted and tested in bottom-illumination setup. Laser pulse repetition frequency is tuned to match the second cantilever resonance, ~180 kHz. In Figure 5.4a and b, normalized spectra of the two functionalized tips are plotted in black. The red curves in Figure 5.4a and b shows the reference spectra measured with reflection absorption infrared spectroscopy (RAIRS) for the same monolayer material on gold substrate[71,72]. They are in excellent agreement with the corresponding photoexpansion spectra of the functionalized tips. For EG6OH, the absorption peak centered at 1,345cm^{-1} and 1,245 cm^{-1} are assigned to –CH_2- wagging and twisting mode respectively. And for NTP, the strong peak around 1,340 cm^{-1} corresponds to the –NO_2 stretching mode. Scanning electron microscopy (SEM) pictures of the two functionalized probes are presented in Figure 5.4c, d, which verified the 10~20-nm tip radii. We estimate that fewer

than ~100 molecules contribute to the measured REINS spectra, within the ~2-nm-radius hotspot as the simulated result in Figure 5.1b.

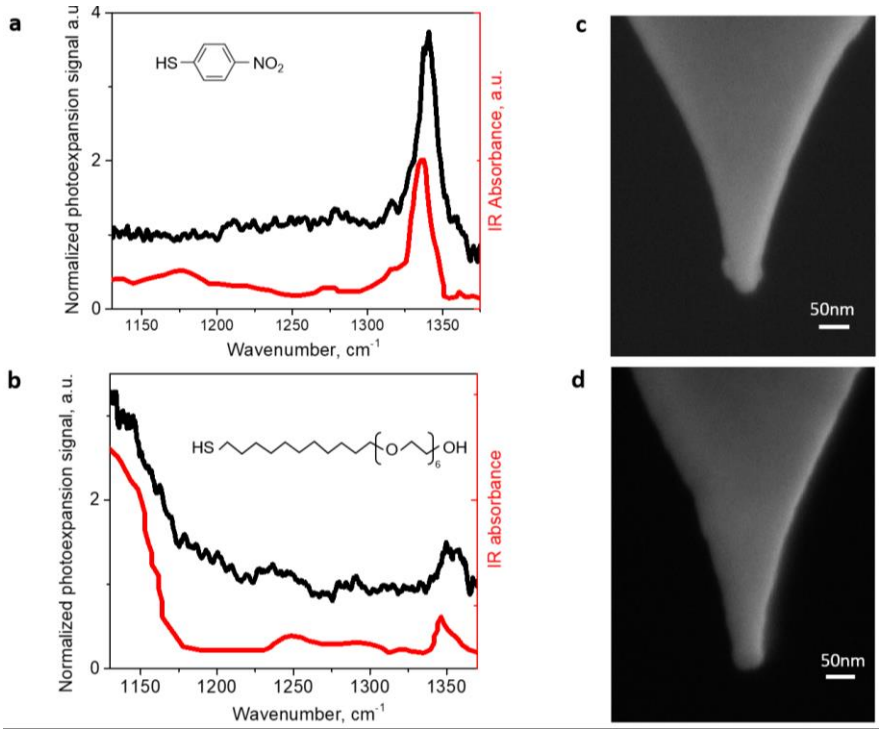

Figure 5.4: Photoexpansion spectra and tip SEM images. **a,** Photoexpansion spectra of NTP functionalized tip and the RAIRS spectrum of NTP SAMs on gold[72] (red); **b,** SEM image of NTP functionalized AFM tip; **c,** Photoexpansion spectra of EG6OH functionalized tip and the RAIRS spectrum of EG6OH SAMs on gold[71] (red); **d,** SEM image of EG6-OH functionalized AFM tip.

However, the molecules on the tip shaft and cantilever as depicted in Figure 5.2 is partially illuminated by far-field evanescent light on the cantilever and tip shaft, which may possibly generate photoacoustic signal[100] and interfere with the photoexpansion signal emerging from the tip apex. Therefore, we measured the spectra with tip retracted from

substrate to verify that the signal solely comes from the tip apex, instead of photoacoustic vibration from the far field absorption of SAMs on tip body and cantilever. As predicted in Figure 5.1b, c, the nearfield optical intensity will drop ~100 times when the tip is retracted from the substrate. We first align the optical path with a functionalized tip and take photoexpansion spectra are shown in Figure 5.5a, b in red. After that, we lift the tip by 100 nm above the prism surface and tune the laser repetition rate to search for the free standing cantilever mechanical resonance. We then scan the laser wavelength and take the "retracted" spectra (shown in Figure 5.5a, b in black). Both NTP and EG6-OH functionalized tips showed more than 10 times lower amplitude without any molecular vibrational absorption bands, which proved that photoacoustic effect induced by molecular laser absorption is negligible in this case and the photoexpansion signal emerges only from the molecules at the tip apex.

In addition, a de-functionalization process is followed by fully oxidizing the SAM layer on functionalized probes in oxygen plasma. Photoexpansion spectra are taken immediately after the cleaning process as plotted in blue curve in Figure 5.5a and b. The absorption peaks of both functionalized tips disappeared, and the signal level away from the absorption peak remains similar as previous, which indicates the probe responsivity to laser is unchanged during the functionalization and O_2 plasma cleaning.

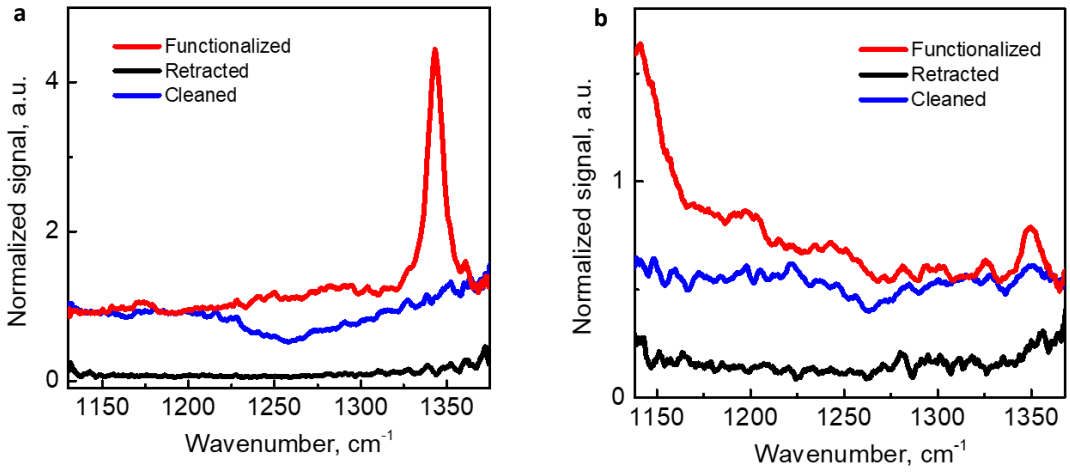

In the simulation, we built the AFM tip as a gold cone with spherical tip apex of 20-nm tip radius. The SAM is modeled as a uniform 1-nm-thick layer covering the apex of a gold tip. The tip is illuminated via the evanescent field of the light illuminated through the germanium prism. The thermal parameters of the materials involved in the simulation are similar to our previous papers[10,41]. We choose the thermal conductivity of gold, germanium and SAM layer to be 314, 60.2 and 0.2 W· (m·K)$^{-1}$ respectively, and the heat capacity to be 129, 310 and 1460 J·(kg·K)$^{-1}$.

Figure 5.5: Photoexpansion spectra of **a,** NTP and **b,** EG6OH functionalized tips in contact with prism (red), retracted from prism (black) and cleaned in O2 plasma (blue)

In conclusion, we experimentally demonstrated the capability of REINS technique to measure vibrational absorption spectra of as few as ~100 molecules on the tip apices of functionalize AFM probes. The results show that REINS technique may potentially be used to measure changes in the vibrational absorption signatures of molecules on the

functionalized AFM tip apices due to nanoscale reactions[87], molecular conformational changes[95–97] and molecular interactions, such as hydrogen bonding [101–103].

Chapter 6 Mid-IR s-NSOM with self-mixing effects in quantum cascade lasers

Quantum cascade lasers (QCLs) are semiconductor lasers based on inter-subband transition that can provide up to watt-level optical power output in infrared (IR) spectral ranges. They have been widely applied as narrow-band mid-IR to far-IR light sources in various systems for sensing, imaging and spectroscopy. Recently, the idea of using QCLs as both the optical source and intra-cavity homodyne interferometric detector has been proposed and experimentally demonstrated, termed as "self-mixing"(SM) [53–60,104,105].

In the self-mixing scheme, the light scattered from a remote target is fed back into the semiconductor laser, which also serves as the illumination source. The coherent detection principle of the SM scheme results in high sensitivity, and detection of optical phase and amplitude detection at the same time. SM detection with an impressive 48 dB optical power attenuation has been achieved recently in THz QCLs by P. Dean et al [56], and they later implemented THz s-NSOM (s-NSOM) with QCLs used as self-mixing detections [58,60]. Recently, M. Giodano has demonstrate THz QCL s-NSOM with SM detection, with 60~70 nm spatial resolution[60].S-NSOM is a powerful tool in mapping the local permittivity and electromagnetic field intensity beyond the infrared diffraction limit. In an s-NSOM setup, an oscillating sharp metal probe of an Atomic Force Microscope (AFM) is brought in close proximity of the sample and illuminated with laser light. The "optical nanofocusing" at the apex of the "antenna-like" tip[106] and the modulation of tip-sample distance causes oscillation in the phase and amplitude of the near-field scattered optical signal. By collecting and analyzing the scattered optical signal, one will extract local optical information of the sample with nanoscale spatial resolution.

Among all the measurement methods of scattered signal in s-NSOM, the self-mixing detection is special in that it dispenses with any IR detectors. The maximum speed of SM response is determined by the lifetime of the upper lasing state, only limited by the elastic and inelastic relaxation mechanisms of a few picosecond[56,107], which makes it a competitive fast mid-IR detector compared to widely-used HgCdTd (MCT) detectors of nanosecond-level response time. Furthermore, the collection of amplitude and phase of the scattered field can be achieved without optical interferometric setup and mechanically moving components. Moreover, the technique can potentially be combined with dual comb spectroscopy, where the multi-heterodyne beat note between two QCL frequency combs can be measured via the self-detection voltage[108,109]. To sum up, our setup result in a compact interferometric infrared sensing and imaging, ready for the QCL-based frequency-comb operation.

6.1 THEORETICAL BACKGROUND FOR QCL SELF-MIXING AND S-NSOM

6.1.1 Self-mixing effects in semiconductor lasers

In the SM scheme, the light scattered from a target is fed back into the semiconductor laser used as the illumination source. As a result, the interference between the back-scattered light with the intra-cavity light introduces a perturbation to the intra-cavity power. This causes the variation in the intra-cavity carrier numbers and results in a change in the device operating voltage (ΔV). The analysis of the optical feedback has been carried out using Lang-Kobayashi equations (See Appendix B) in previous studies[53–55,104,110]. The following simple expression of emitted laser power can be assumed:

$$P(\varphi) = P_0(1 + m \cdot F(\varphi)) \tag{6.1}$$

where P_0 is the laser power without any feedback perturbation. m is the amplitude modulation index and $F(\varphi)$is a periodic function of the feedback phase shift $\varphi = 4\pi L\lambda^{-1}$. Here L stands for the external cavity length and λ represents the laser wavelength. Both m and $F(\varphi)$ depends on the *feedback parameter C* as:

$$C = \frac{\kappa \cdot L}{n \cdot l}\sqrt{1+\alpha^2} \tag{6.2}$$

Here n and l are the refractive index and length of the laser cavity respectively. α is the laser linewidth enhancement factor (α is taken as 0 for simplicity in the following calculation). The factor κ is given by:

$$\kappa = \varepsilon \cdot r_{ext} \cdot \frac{1-R_2}{R_2} \tag{6.3}$$

where $r_{ext} = \sqrt{R_{ext}} < 1$, is the square root of total power reflectivity R_{ext} of the remote target, representing the amplitude ratio between the back-scattered field and emitted field. R_2 is the reflectivity of the laser output facet. For the uncoated quantum well facet, the reflectivity R_2 = 0.27, calculated from a typical refractive index of 3.2 for normal light incidence. The factor $\varepsilon \leq 1$ accounts for the coupling mode mismatch between feedback light and lasing mode (ε is assumed as 1 in the following calculations).

C parameter is significant in self-mixing detection experiments, as different feedback regime are classified based on its value.

Solving the Lang-Kobayashi equations yields the equation:

$$\omega_F(\tau)\cdot\tau = \omega_0 \cdot \tau - \frac{C}{\sqrt{1+\alpha^2}}\left\{\alpha \cdot \cos\left[\omega_F(\tau)\cdot\tau\right] + \sin\left[\omega_F(\tau)\cdot\tau\right]\right\} \tag{6.3}$$

where $\tau = \frac{2L}{c}$ is the photon round-trip time in the external cavity (c is the speed of light in free space), and ω_0 and $\omega_F(\tau)$ are the angular frequency of the laser emission without and with optical feedback respectively. According to Equation (6.3), the equation only have one solution when $C < 1$, but multiple solutions when $C \geq 1$.

The modulation index m and function $F(\varphi)$ is determined by:

$$m = C \cdot \frac{2 \cdot \tau_p \cdot c}{L\sqrt{1+\alpha^2}} \tag{6.4a}$$

$$F(\varphi) = \cos\left[\frac{\omega_F(\varphi)}{\omega_0} \cdot \varphi\right] \tag{6.4b}$$

Here $\tau_p = -\frac{2 \cdot n \cdot l}{c \cdot \log(R_1 \cdot R_2)}$ is the intra-cavity photon life time at steady state. R_1~1, is the reflectivity of the other laser facet, usually coated with anti-reflection coating.

In the weak feedback regime[53,54] (C < 0.1), according to Equation (6.3), the perturbed laser frequency $\omega_F \approx \omega_0$. As a result, the function $F(\varphi) \approx \cos(\varphi)$ and the perturbed laser power has the form $P(\varphi) = P_0(1 + m \cdot \cos\varphi)$. In other words, the power variation has sinusoidal waveform:

$$\frac{\Delta P}{P_0} = \frac{P - P_0}{P_0} = m\cos\varphi \tag{6.5}$$

Using small signal approximation, the QCL voltage change is proportional to the carrier variation induced by intra-cavity power variation. From the Lang-Kobayashi equation, it can be described by the following equation[53–55]:

$$\Delta V \propto r_{ext}\cos\varphi \tag{6.6}$$

6.1.2 Near-field scattering by a nanoscale metal particle

To study the scattering field of a sharp metalized AFM tip, we can equivalently modeled the tip as a metal spheroid as shown in Figure 6.1. Once the spheroid is brought close to the sample surface, the dipole starts to couple with its image dipole in the sample, leading to the effective polarizability for the tip-sample system:

$$\alpha_{eff} = R^2 L \frac{L(\varepsilon_t - 1)(2L\sqrt{1-R/L} + R\ln\frac{(1-\sqrt{1-R/L})^2}{R/L})}{2L\sqrt{1-R/L}(L - R\varepsilon_t) - RL(\varepsilon_t - 1)\ln\frac{(1-\sqrt{1-R/L})^2}{R/L}} \cdot (2 + \frac{\beta(gL - R - d)\ln\frac{L}{d + 3R/4}}{(d - gL + 3R/4)\beta\ln\frac{L}{d + R/2} + L\ln(4L/R)}) \tag{6.7}$$

where R and L_t ($2L_t << \lambda$) are the parameters representing the tip geometry as shown in Figure 6.1. ε_t is the permittivity of the tip material. For the gold-coated tip used in our setup, skin depth of gold $\delta_{sd} = \lambda / \left(2\pi \operatorname{Im}\sqrt{\varepsilon_{Au}}\right) \approx 23nm$ is smaller than the nominal coating thickness 70nm, ε_t is assumed to be the permittivity of the gold $-3411 + 514.7i$. $\beta = (\varepsilon_s - 1)/(\varepsilon_s + 1)$, where ε_s is the permittivity of the sample. d is the tip-sample spacing as shown in Figure 6.1. g is a constant parameter smaller than 1. Based on Equation 6.7, the tip-sample scattering depends on both the local sample permittivity and the tip-sample distance.

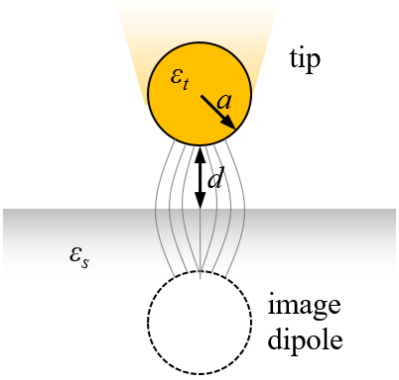

Figure 6.1: Modeling of the near-field interaction in s-NSOM. The scattered light field is dependent on the tip-sample spacing d and the local sample permittivity ε_s.

The scattered far field $E_{sca} = \sigma E_{in} \propto \frac{\alpha_{eff}\pi}{\lambda^2}\sqrt{\frac{8}{3}}E_{in}$ (σ is related with the scattering cross-section of the metal particle based on the Mie scattering theory, see Appendix A) directly measures the amplitude s and phase ψ of the near-field scattering coefficient $\sigma = s \cdot e^{i\psi}$.[111]

In self-mixing detection, the voltage signal ΔV will have the following form:

$$\Delta V = s\cos(\psi + \varphi) \tag{6.9}$$

In this equation, $\varphi = 4\pi L\lambda^{-1}$ is the round-trip phase shift in the external cavity, and $\psi + \varphi$ stands for the total phase shift between the intra-cavity mode and the feedback light.

In practice, the AFM tip is dithering at its tapping frequency Ω near its mechanical resonance mode. This causes a sinusoidal motion of the tip-sample distance d, $d' = d + d_0(\sin\Omega t + 1)$, leading to the modulation of α_{eff} at frequency Ω. Due to the nonlinear dependence of σ on tip-sample distance d, the scattering coefficient can be decomposed into a Fourier series:

$$\sigma(\Omega t) = s_0 e^{i\psi_0} + s_1 e^{i\psi_1} e^{i\Omega t} + s_2 e^{i\psi_2} e^{2i\Omega t} + \ldots + s_n e^{i\psi_n} e^{ni\Omega t} \qquad (6.10)$$

For a 20-nm-radius gold particle oscillating on gold substrate with 20 nanometer amplitude, the *s* Fourier coefficients is calculated and plotted as a function of the tip sample distance *d* in Figure 6.2.

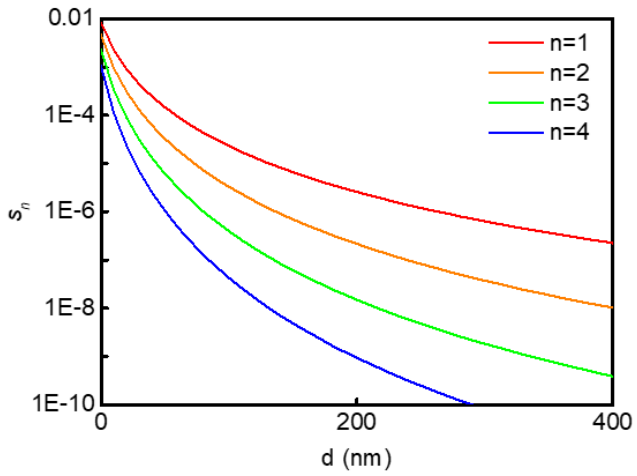

Figure 6.2: Scattering amplitude s_n at the nth harmonic of modulation frequency Ω as a function of tip-sample distance *d*.

With the demodulation on the lock-in amplifier, the voltage signal ΔV_n at the *n*th harmonic order can be measured independently.

Experimentally, as the size of the focal spot is on the order of ~50μm, there is background scattering from the sample surface and tip cantilever. There are two methods to suppress the background signal interference.

The background signal $s_{0b} e^{i\psi_{0b}}$ from the sample surface is strong but not modulated with the tip frequency, which is an additional term for the scattering coefficient in Equation (6.10) ($s_{0b} >> s_1, s_2 \ldots$). Considering Equation (6.10), the coupling between

laser output light and feedback light has the same expression as a homodyne interferometer[33,112]:

$$\Delta V_n \propto s_0 s_n \cos(\psi_n - \psi_0) + s_n \cos(\psi_n + \varphi) \tag{6.11}$$

Here $s_0 s_n \cos(\psi_n - \psi_0)$ is a constant term for a given tip-sample scattering system, independent of round-trip phase shift φ. By plotting ΔV_n as a function of φ, one could obtain the amplitude s_n and phase ψ_n of nth order scattering coefficient.

Secondly, scattering light signal at higher harmonics of Ω is preferred, as the scattering at the tip shaft and cantilever tends to decay faster than near-field scattering with increasing harmonic order.[36,111,113] As a result, the near-field scattering signal becomes more dominant at high harmonics.

6.1.3 Background-free phase and amplitude imaging using SM detection

In an SM image, the SM voltage signal ΔV_n is set as the pixel intensity, which has an offset due to background scattering signal. According Equation (6.11), phase ψ_n and amplitude s_n at can be obtained by fitting the sinusoidal waveform of ΔV_n. However, it would be time consuming if we need to perform that for each pixel in an image, which generally contains thousands of pixels. Here we propose the image subtraction approach similar to the s-NSOM homodyne detection[112]. Assuming we have a simple sample, which is composed of two types of material, *A* and *B*. The self-mixing voltage signal measured at the nth harmonic is $\Delta V_{A,n}$ and $\Delta V_{B,n}$ respectively. When the tip is placed on top of material A, by adjusting the external-cavity round-trip phase shift $\varphi = 4\pi L\lambda^{-1}$, we can let $\cos(\psi_{A,n} + \varphi)$ equal to 1, 0 or -1 at φ_1, $\varphi_1+\pi/2$ and $\varphi_1+\pi$ respectively. After that, we take

three SM images consecutively at identical image location at these three phase shift values, namely M_n^1, $M_n^2$and M_n^3. By performing pixel-wise image subtraction, we will obtain:

$$u_n = \frac{M_n^1 - M_n^3}{2}$$

$$v_n = \frac{M_n^1 + M_n^3}{2} - M_n^2$$

$$\sigma_n \propto u_n + i \cdot v_n \tag{6.12}$$

Hence the phase and amplitude image can be generated by calculating the angle and modulus of the complex value $u_n + i \cdot v_n$. Accordingly, on the phase image of the sample, the phase is 0 on material A and $\psi_{B,n}$ - $\psi_{A,n}$ on material B.

6.2 EXPERIMENTAL SETUP

The schematic drawing of the experimental setup is shown in Figure 6.3a. A single mode CW QCL with 8.6 μm wavelength is used as the light source and detector. From Figure 6.2b, the laser current threshold $I_{th} = 540mA$. The laser current is controlled by *I* source (Lightwave IDX3232 low-noise current source), typically set at 575*m*A for SM detection, 6% above I_{th}. BS stands for a 50/50 CaF_2 beam splitter and L1,L2 are two IR lenses. About 6*m*W radiation from the QCL is collimated by L1 (NA=0.7) and focused onto the tip apex by L2 (NA=0.5), with ~60° incident angle relative to the surface normal. Light polarization is set along the tip shaft. The tip is dithering in sinusoidal motion with frequency Ω (~70kHz) along the z-direction and the tip driving voltage is fed into a lock-in amplifier as the reference signal. Back-scattered light is sent into the QCL cavity along

the same path as the incident beam. The voltage signal across QCL is first filtered with a bias tee diplexer to remove the DC voltage offset. The RF output from bias tee is connected to the lock-in amplifier signal channel to obtain the *n*th SM voltage signal. Additionally, half of the back-scattered light is sent into an HgCdTd (MCT) detector for comparison with SM signal. A fraction of the laser emission is also directed to a power meter (PM) for laser power monitoring. The instruments in the shaded area in Figure 6.3a is merely designed to provide a reference, which is an optional feature, not interfering with the SM detection. The distance from the QCL output facet to the AFM tip is L~19cm. The length of the laser l =2mm and the refractive index of the laser cavity n = 3.2.

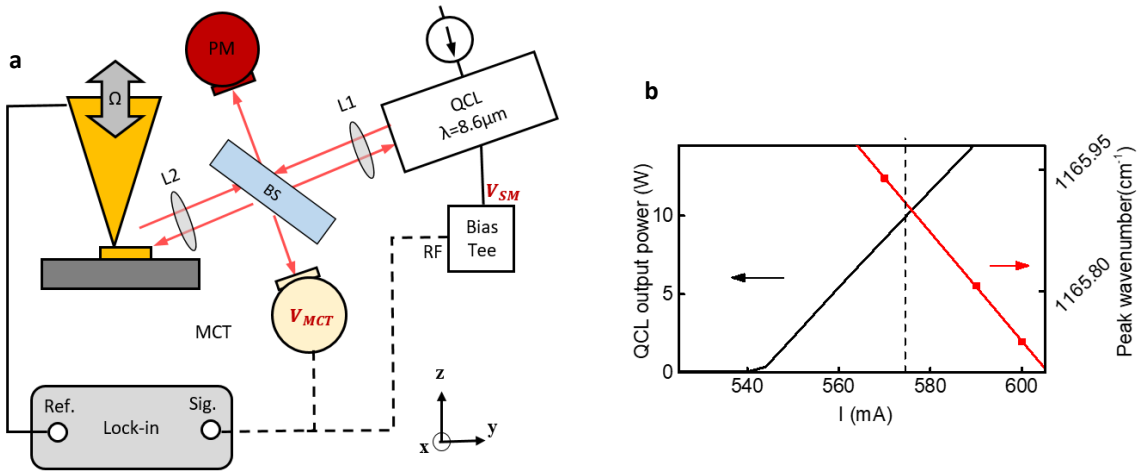

Figure 6.3: **a**, Experimental setup of mid-IR QCL s-NSOM self-mixing detection; **b**, Black curve: QCL L-I curve without optical feedback; Dashed line: operating laser current for SM detection; Red line: center wavelength of laser emission as a function of current.

Interestingly, the laser number of the CW QCL source has linear tunability with laser driving current, with a tuning rate of $\frac{d(\lambda^{-1})}{dI} = -6.68\times10^{-3} cm^{-1}/mA$, as depicted in

red in Figure 6.3b. The reason is the different level of QCL heating under different driving currents produces a minor variation in the intra-cavity refractive index, which results in the shift in the laser Fabry-Pérot mode. Consequently, we can achieve phase tuning of $\Delta\varphi = \pi$ by varying the laser driving current by ~2*m*A.

6.3 PHASE AND AMPLITUDE IMAGING BY S-NSOM SM DETECTION

We prepared some gold film on dielectric substrate via lift-off processes for the proof-of-concept demonstration.

6.3.1 Measurement of *C* parameter

It is important to make sure the SM systems is operating in the weak feedback regime, so that the approximation in the above analysis is valid. Although the modulated near-field scattering of the tip-sample interaction is weak, the DC background light scattered from the sample surface might be strong. In order to determine the *C* parameter, we performed the measurement based on Equation (6.5). The AFM tip is oscillating above a gold sample surface. The reading of the power meter with optical feedback *P*, and without feedback P_0 are measured at a set of different laser driving currents. And we plot the normalized power variation $\frac{\Delta P}{P_0} = \frac{P - P_0}{P_0}$ a function of current as shown in Figure 6.4. As the laser wavenumber has linear tunability on the laser driving current, the external-cavity round-trip phase shift $\varphi = 4\pi L\lambda^{-1}$ is linearly scaled with the current, which allows the normalized power variation to have the complete sinusoidal waveform predicted by the $\cos\varphi$ term in Equation (6.5). From the figure, the oscillation amplitude of the sinusoidal wave *m* reads 0.0046. Given Equation (6.4a), *C* is calculated to be 0.045 < 0.1 in this setup.

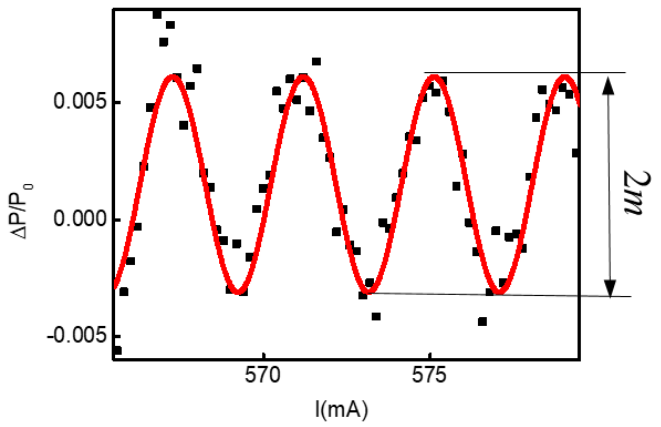

Figure 6.4: Normalized laser power variation as a function of laser current.

6.3.2 SM phase and amplitude signal

The topography of the boundary of 50-nm-thick gold film deposited on fused silica substrate is presented in Figure 6.5a. We connect the QCL voltage signal to the lock-amplifier and select the harmonic order to measure. Figure 6.5b and Figure 6.5c are SM voltage signal demodulated at Ω and 2Ω respectively. The image was taken with lock-in integration time of 30ms and the AFM scan rate of 0.15Hz. Figure 6.5d and Figure 6.5e are reference signal recorded with MCT output voltage demodulated at Ω and 2Ω scanning over the same area. SM voltage signal shows clear contrast on gold and on silica, which is in good agreement with the MCT reference signal. The 2nd order SM voltage signal measures $\Delta V_2 \propto s_0 s_2 \cos(\psi_2 - \psi_0) + s_2 \cos(\psi_2 + \varphi)$, with tunable φ. However the 2nd order MCT signal measures the scattered field amplitude, $\Delta V_{MCT,2} \propto 2 s_0 s_2 \cos(\psi_2 - \psi_0) + s_1^2$.

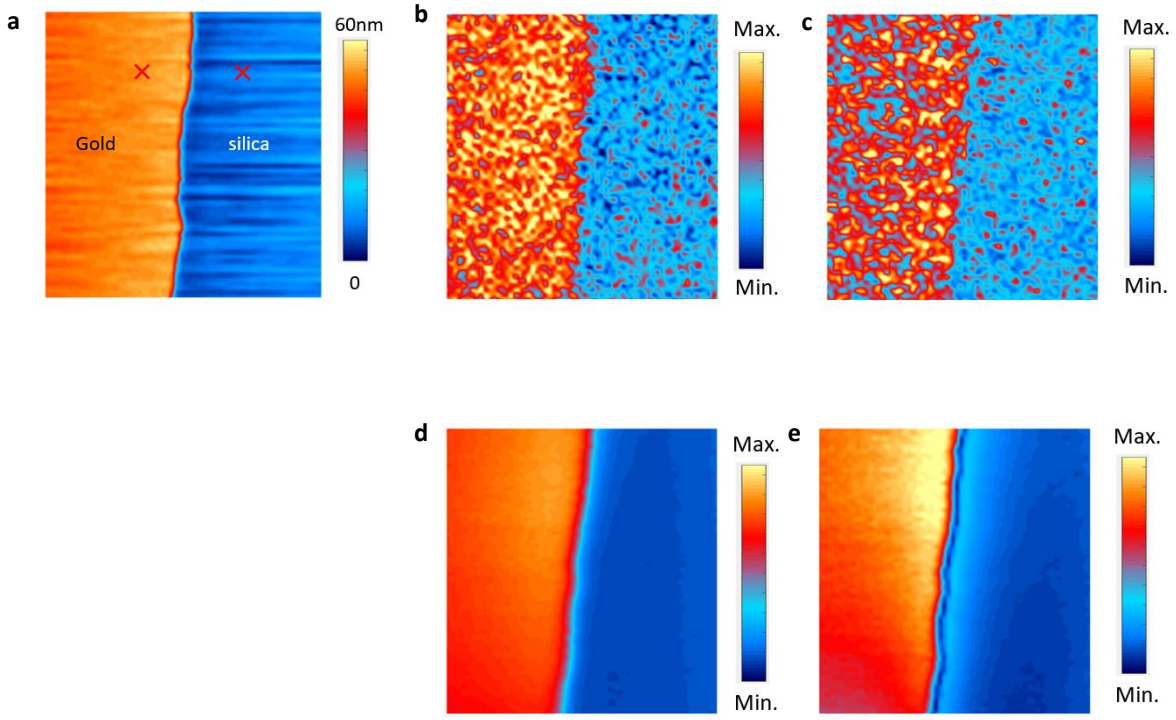

Figure 6.5: **a**, AFM topography of 50-nm-thick gold film on fused silica substrate; **b**, SM voltage signal ΔV_1 collected at with demodulation frequency Ω; **c**, SM voltage signal ΔV_2 collected at 2nd harmonic frequency 2Ω; **d**, MCT signal at collected at with demodulation frequency Ω; **2**, MCT signal at collected at with demodulation frequency 2Ω. All images are 2μm × 2μm size.

The phase and amplitude on gold and fused silica are measured with a set of laser driving currents at two locations marked by the red crosses in Figure 6.5a. The current is converted to the external cavity round-trip phase shift $\Delta\varphi$, by $\Delta\varphi = 4\pi L \cdot \left(\frac{d\lambda^{-1}}{dI}\right) \cdot (I - I_0)$, assuming the phase shift at I_0 =585mA is the initial zero-point. Let the scattering coefficient of gold and silica be $\sigma_{Au} = s_{Au} e^{i\psi_{Au}}$ and $\sigma_{silica} = s_{silica} e^{i\psi_{silica}}$ respectively. From Figure 6.6b,

the amplitude ratio $\frac{s_{Au,2}}{s_{silica,2}} = 4.2$ and the relative phase shift $\psi_{Au,2} - \psi_{silica,2} = 0.2\pi$ at the two locations.

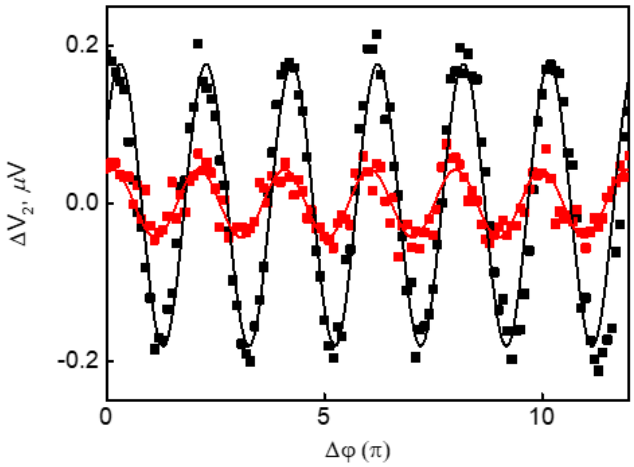

Figure 6.6: SM signal demodulated at 2Ω ΔV_2 on gold (black curve) and fused silica (red curve), respectively.

Phase and amplitude imaging on the same sample is demonstrated on 2μm × 1μm area presented in Figure 6.7. Figure 6.7a shows the AFM topography of the boundary of the gold film. Figure 6.7b,c are amplitude and phase image at frequency Ω obtained with image subtraction method. Figure 6.7d,e are the amplitude and phase image obtained at frequency 2Ω. The images displays the contrast on gold and silica, which is also in good agreement with the phase shift measured at two locations in Figure 6.6.

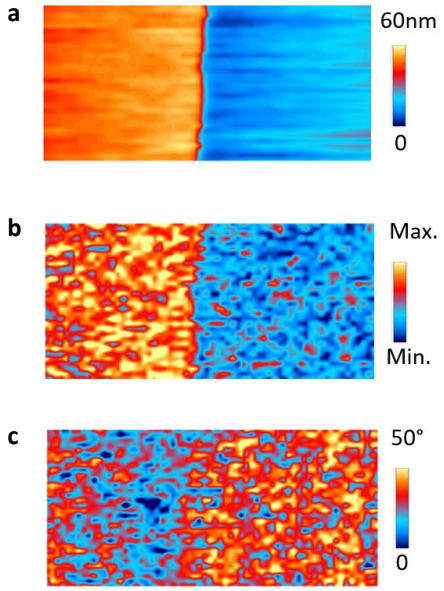

Figure 6.7: **a**, AFM topography of 50-nm-thick gold on fused silica substrate; **b**, amplitude and **c**, phase image of the self-mixing signal at 2Ω frequency. The image is 2 μm × 1 μm in size with 64 × 32 pixels.

Phase and amplitude imaging on the same sample is demonstrated on 2μm × 1μm area presented in Figure 6.7. Figure 6.7a shows the AFM topography of the boundary of the gold film. Figure 6.7b,c are amplitude and phase image at frequency 2Ω obtained with

image subtraction method. The images displays the contrast on gold and silica, which is also in good agreement with the phase shift measured at two locations in Figure 6.6.

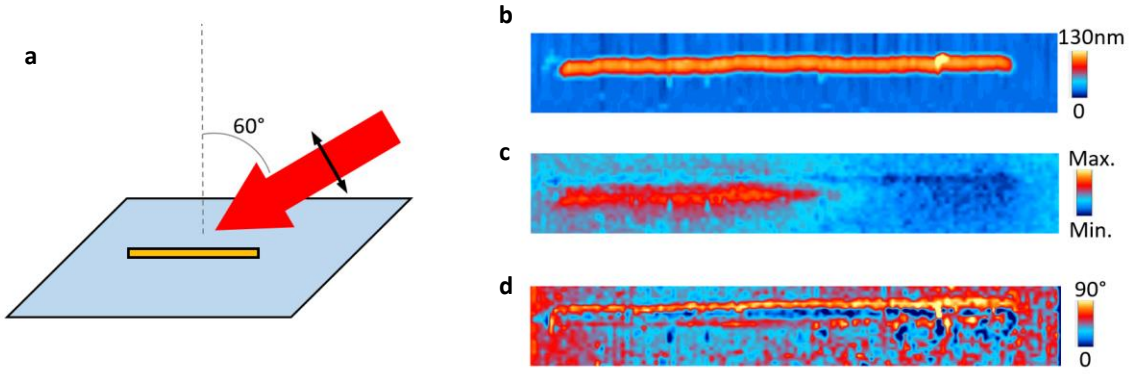

Figure 6.8: **a**, The *p*-polarized laser incident angle is 60 degrees relative to the surface normal. The projection of the laser beam on the sample plane is parallel to the gold antenna. **b**, AFM topography of a single gold nano-wire with 130 *nm* in width and 3 μm in length on Al_2O_3 substrate; **c**, SM amplitude and **d**, SM phase images at frequency Ω. The images in **b**,**c** and **d** are 4 μm × 0.75 μm in size with 128 × 24 pixels.

In order to demonstrate our ability of imaging nanostructures, we fabricated gold nano wires on Al_2O_3 substrates using electron beam lithography. The nano wire is 3 μm in length and 130 *nm* in width. The images show a transition of near-field scattering amplitude and phase when the tip moves from one end of the wire to the other.

To summarize, we demonstrated s-NSOM using QCL self-mixing detection on gold film on dielectric substrate in the weak feedback regime. The phase and amplitude measurement was achieved via self-mixing homodyne detection and laser wavelength tuning by the driving current. The SM phase and amplitude imaging was completed with

lock-in demodulation frequency at Ω and 2Ω. The system results in simple and robust setup, without the need of any photodetectors and mechanical moving parts.

6.4 DISCUSSION AND FUTURE IMPROVEMENTS

As the fast development of QCL sources, new methods of self-mixing detection configurations are conceived and studied, for the sake of compact, fast, room-temperature, broadband and detector-free devices.

6.4.1 Measurement of *C* parameter from SM voltage

C parameter is directly proportional to the laser power modulation index *m*. As a result, it is straightforward to calculate *C* parameter from the normalized laser power output variation. From Lang-Kobayashi equations, it is possible to extract *C* parameter from the self-mixing voltage, and thus further suppress the need for optical power meters which has slow response time. The relation between the SM voltage and *C* parameter can be interpreted using the Boltzmann's law of carrier concentration produced by a bias voltage *V*[55]:

$$N = N_0 \cdot e^{\frac{eV}{2k_B T}} \tag{6.13}$$

Here N0 is the carrier concentration at equilibrium (*V*=0). *e* is the electron charge, k_B is the Boltzmann constant and T is the temperature. After plugging this equation in the Lang-Kobayashi equations and performing proper approximation, the SM voltage change $\Delta V = V - V_0$ (V_0 is the unperturbed laser voltage) can be expressed as:

$$\Delta V = -\frac{1}{r_{ext}} \frac{\sqrt{2} k_B T}{e} \chi \cdot \cos\varphi \tag{6.14}$$

where $\chi = (G_t N_t \tau_p)^{-1}(2\gamma l + \ln R_1 R_2)^{-1}$ is constant for a given QCL SM detection system. G_t and N_t is the carrier concentration are the gain factor and carrier concentration at laser transparency, respectively. γ is the power gain in unit active region and l is the laser cavity length. It is not easy to obtain the value of χ directly from these parameters. But we can measure the amplitude of the SM voltage signal in a SM detection system with known external cavity reflectivity $r_{ext}^{\ 2}$, and find out the χ value accordingly.

Figure 6.9 presents the SM voltage signal measured simultaneously with Fig 6.4. The self-mixing voltage signal is produced by strong background scattering from the sample other components in the imaging system. The laser wavelength tuning by the driving current causes the variation in φ in Equation (6.14). From the Figure, the amplitude of ΔV is 0.23mV. If our estimation of the C parameter of 0.045 in Section 6.3.1 is correct, $r_{ext} \approx 2.4\times10^{-3}$, and thus $\frac{\sqrt{2}k_B T}{e}\chi \approx 0.56$. We will have $\Delta V = -\frac{0.56}{r_{ext}} \cdot \cos\varphi$.

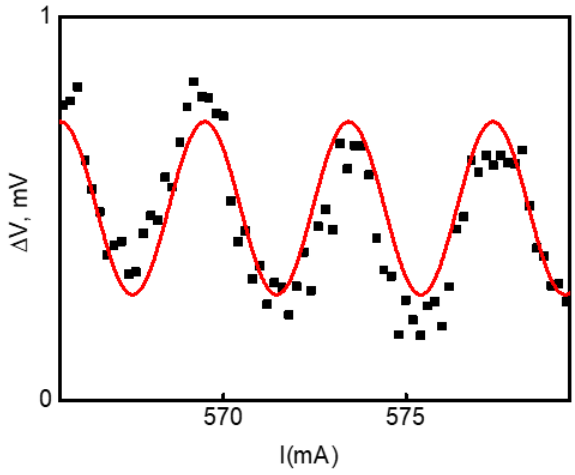

Figure 6.9: SM voltage signal ΔV as a function of laser driving current.

6.4.2 Phase and amplitude of theoretical models

The phase and amplitude of the theoretical models can be calculated using the models described in Equation 6.7. Based on the typical values of the AFM tips[114], we take R=20 nm, Lt =350 nm. We set permittivity of the samples $\varepsilon_{Au} = -3412 + 519i$ and $\varepsilon_{SiO2} = -1.23 + 0.886i$. The constant g is taken as $g = 0.85e^{0.08i}$. The tip sample distance $d = (20 + 20\sin\Omega t)nm$, which represents 20 nm tip oscillation amplitude above the sample surface. By plugging in the parameters and taking the Fourier Transform of Equation (6.7), we are able to calculate the scattering coefficient at different harmonic orders. For the second harmonic order, the amplitude ratio $\frac{s_{Au,2}}{s_{silica,2}} = 3.3$ is close to the experimental value of 4.2, which is discussed in section 6.3.2.

6.4.3 SM detection in s-NSOM with QCL frequency combs

Self-mixing detection has been applied for dual-comb spectroscopy using QCL frequency combs[108,109,115]. IR frequency comb has been successfully generated in mid-IR and THz range by four-wave mixing[116–119] or via dispersion compensation structures[120]. With the broadband IR frequency comb as the light source, one is able to measure the spectrum at the same time, without the need to tune the wavelength. In this section, some preliminary analysis of using frequency combs for SM detection in s-NSOM systems is performed.

It is not easy to achieve broadband comb spectroscopy using a single QCL as both the frequency comb source and detector for SM detection in s-NSOM. Assuming we have

a QCL comb, with ω_0 as the lowest comb frequency, and Δ as the comb spacing. The feedback comb beating with the emitted comb will produce beat signal at multiple harmonics of Δ. However the beat signal at $N\Delta$ is the sum of all combinations of comb pairs which has difference frequency at $N\Delta$. It is almost impossible to distinguish each of them if we have a broadband comb.

Assuming we have two CW QCLs, emitting IR frequency combs with different comb spacing. One of them has the lowest comb at ω_0 with comb spacing Δ. And the other one starts at $\omega_0+\delta_s$, with comb spacing $\Delta+\delta$ ($\delta>\delta_s$). If we use one of the QCL comb as the light source of an s-NSOM system, and feed the reflected signal into the other QCL comb, we would be able to measure the voltage beat note at multiples of frequency δ, which is known as dual-comb spectroscopy.

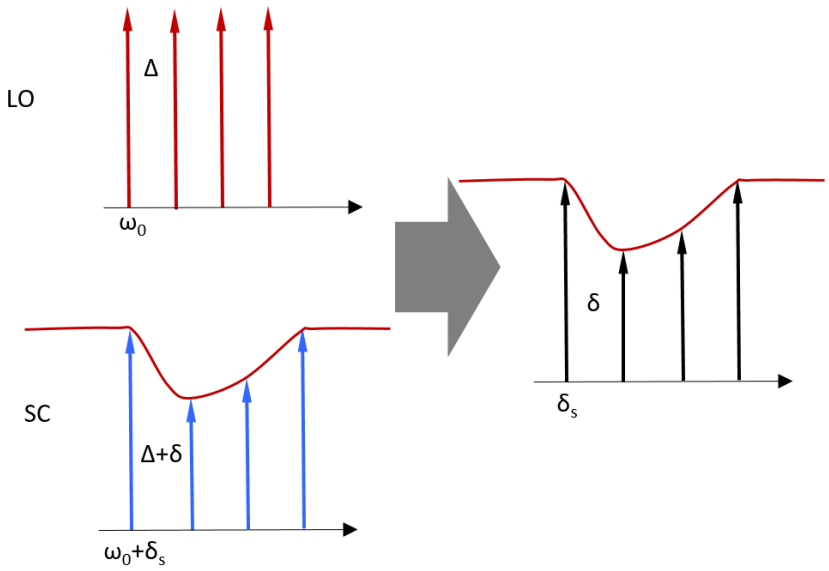

Figure 6.10: Dual-comb spectroscopy performed by mixing between the sample comb and the local oscillator.

A first-step on-chip QCL dual-comb spectroscopy has been demonstrated by Villares *et al.*[108], using a QCL comb as the light source and the other QCL comb as the detector. The comb spacing and offset tuning was controlled by temperature tuning of the refractive index. According to the s-NSOM scattering theory, on-chip QCL dual-comb spectroscopy can be applied to analyze the amplitude and phase of near-field scattered field. The detection mechanism of QCL self-mixing dual-comb spectroscopy is elaborated below.

Let the optical field amplitude at the *X*th comb tooth of the first comb equal to: $E_1^{(X)}e^{i[\omega_0+\delta_s+X(\Delta+\delta)]t}$ and the field of the corresponding comb tooth in the second comb as: $E_2^{(X)}e^{i(\omega_0+X\Delta)t}$. By using the first comb as the light source, the feedback field at the *X*th tooth of the scattered light comb can be expressed as $E_F^{(X)} = E_1^{(X)}e^{i[\omega_0+\delta_s+X(\Delta+\delta)]t}\cdot\sigma_{eff}^{(X)}e^{i\varphi^{(X)}}$. Here $\sigma_{eff}^{(X)} = s^{(X)}e^{i\psi^{(X)}}$ is the near-field scattering coefficient and $\varphi^{(X)} = [\omega_0+\delta_s+X(\Delta+\delta)]\frac{4L}{c}$ is the external-cavity round-trip phase shift of the *X*th comb. With the tip modulation of the near-field scattering, $\sigma_{eff}^{(X)}$ can be written as:

$$\sigma_{eff}^{(X)} = s_{0b}^{(X)}e^{i\psi_{0b}^{(X)}} + \sum_{n=1} s_n^{(X)}e^{i\psi_n^{(X)}}e^{in\Omega t} \tag{6.15}$$

Here we consider the background scattering from the sample surface, and write $s_{0b}^{(X)}e^{i\psi_{0b}^{(X)}} = s_0^{(X)}e^{i\psi_0^{(X)}} + s_b^{(X)}e^{i\psi_b^{(X)}}$ ($s_{0b}^{(X)} >> s_1^{(X)} > s_2^{(X)} > \ldots$) as the sum of background scattering and the zeroth order Fourier series of tip modulated scattering, which are independent of the tip modulation frequency Ω. When $E_F^{(X)}$ is coupled into the second QCL cavity, the mixing between $E_F^{(X)}$ and $E_2^{(X)}e^{i(\omega_0+X\Delta)t}$ will lead to laser intensity change in the second laser, proportional to:

$$\left|E_F^{(X)} + E_2^{(X)}e^{i(\omega_0+X\Delta)t}\right|^2 - \left|E_2^{(X)}\right|^2 \tag{6.16}$$

By neglecting small terms and Ω-independent terms, we will obtain the following expression:

$$\left[E_2^{(X)}e^{i(\omega_0+X\Delta)t}+E_1^{(X)}e^{i[\omega_0+\delta_s+X(\Delta+\delta)]t}s_{0b}^{(X)}e^{i\psi_{0b}^{(X)}}e^{i\varphi^{(X)}}\right]^* E_1^{(X)}e^{i[\omega_0+\delta_s+X(\Delta+\delta)]t}e^{i\varphi^{(X)}}\sum_{n=1}s_n^{(X)}e^{i\psi_n^{(X)}}e^{in\Omega t}+C.C.$$

$$=\sum_{n=1}s_n^{(X)}e^{i\psi_n^{(X)}}e^{in\Omega t}\left[E_2^{(X)*}E_1^{(X)}e^{i(\delta_s+X\delta)t}e^{i\varphi^{(X)}}+\left|E_1^{(X)}\right|^2 s_{0b}^{(X)}e^{-i\psi_{0b}^{(X)}}\right]+C.C.$$

$$=\left|E_2^{(X)*}E_1^{(X)}\right|\sum_{n=1}s_n^{(X)}\cos\left[(\delta_s+X\delta+n\Omega)t+\psi_n^{(X)}+\varphi^{(X)}\right]$$

$$+\left|E_1^{(X)}\right|^2 s_{0b}^{(X)}\sum_{n=1}s_n^{(X)}\cos\left[n\Omega t+\psi_n^{(X)}-\psi_0^{(X)}\right]$$

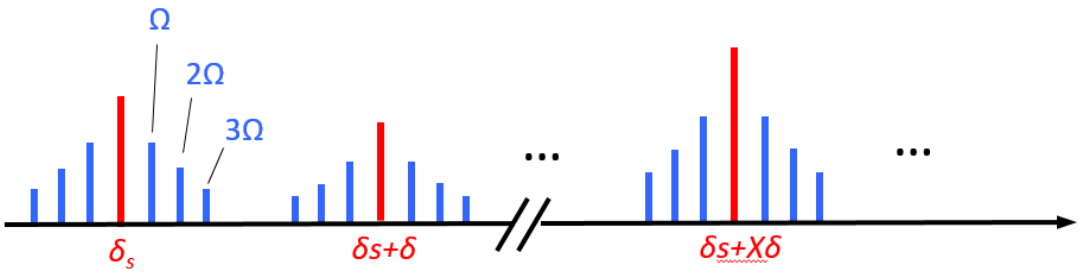

Figure 6.11: Frequency spectrum of the QCL self-mixing dual comb spectroscopy.

As a result, in the frequency domain, the self-mixing voltage signal will present the following frequency spectrum in Figure 6.11. For the *X*th comb tooth of the beat signal at the *n*th harmonic of the tip frequency Ω, the signal amplitude would be:

$$\left|E_2^{(X)*}E_1^{(X)}\right|s_n^{(X)}\cos\left[\psi_n^{(X)}+\varphi^{(X)}\right]+\left|E_1^{(X)}\right|^2 s_{0b}^{(X)}s_n^{(X)}\cos\left[\psi_n^{(X)}-\psi_0^{(X)}\right] \quad (6.17)$$

In the equation, the second term arises from the background scattering from the sample surface, which can be removed in the homodyne interferometric detection method.

Here, the second term does not has dependency on $\varphi^{(X)} = [\omega_0 + \delta_s + X(\Delta + \delta)]\frac{4L}{c}$, which can be tuned independently. In this way, the amplitude $\left|E_2^{(X)*}E_1^{(X)}\right| s_n^{(X)}$ and phase $\psi_n^{(X)}$ of the first term can be obtained. In addition, $\left|E_2^{(X)*}E_1^{(X)}\right|$ spectrum can be measured by using an optical modulator driving at frequency Ω with uniform reflection s_{const} in the comb range as the target sample instead of the near-field probe (for instance, an optical chopper and a metal reflector). Therefore, by normalizing the measured dual-comb spectrum with the $\left|E_2^{(X)*}E_1^{(X)}\right|$ spectrum, the actual amplitude $s_n^{(X)}$ of the near-field scattering at each comb tooth can be calculated.

Chapter 7 Conclusion

In conclusion, we demonstrated a set of experiments on mid-IR near-field nanospectroscopy and microscopy on a variety of samples under different conditions. High quality AFM-IR nanospectroscopy was achieved on ~1nm monolayer thick molecules. The signal is enhanced by cantilever mechanical resonance enhancement and tip lightening rod effect. A spatial resolution of 25 nm was achieved on 2 nm thick sample. Only ~ 300 molecules contribute to the cantilever deflection signal.

AFM-IR nanospectroscopy is also realized on 20-nm-thick PMMA film, with both tip and sample submerged in D_2O environment. The cantilever mechanics in aqueous environment is investigated and analyzed. We overcame the strong water damping effect on AFM cantilever by exciting higher order bending modes of the AFM cantilever. And we suppressed water thermal expansion background by evanescent illumination from a high-index prism near the critical angle. It demonstrates a tool that can potentially be applied to imaging of chemistry and biological samples in their native aqueous environment.

The spectra of tips functionalized with SAM molecules are demonstrated on the prism. The spectra before and after oxygen plasma cleaning verified the signal from monolayer molecules can be measured on dielectric substrates. The functionalized probes can be used for chemical sensing to recognize some specific chemical groups.

Last but not least, s-NSOM can also be performed with a “detector less” scheme, where a QCL laser source is employed as both the light source and homodyne photodetector. The laser scattered by the AFM probe can be sent back into the laser cavity and couple with the intra-cavity light power. The external-cavity round-trip phase tuning

is realized by temperature tuning of the laser emission wavelength. The experimental setup can also work for THz QCLs and QCL frequency combs, which will lead to robust and compact near-field IR imaging tools with broader spectral range.

Appendix A

The scattering cross section C_{scat} in m^2 can be defined as

$$C_{scat} = \frac{W_{sca}}{I_{in}} \tag{A.1}$$

where I_{in} represents the incident light intensity and W_{scat} are the scattered energies integrated over the whole solid angle in the space. Therefore, $C_{scat} \propto \frac{|E_{scat}|^2}{|E_{in}|^2}$ indicates the ratio between the scattered and the incident field intensity.

The famous Rayleigh cross section formula for light scattered from a particle much smaller than the wavelength can be expressed as[121]:

$$C_{scat} = \left(\frac{2\pi}{\lambda}\right)^4 \frac{|\alpha|^2}{6\pi} \tag{A.2}$$

Here α is the polarizability of the sphere denoted in Equation (6.8). As a result, the following relation could be obtained:

$$\frac{E_{sca}}{E_{in}} \propto \pi \sqrt{\frac{8\pi}{3}} \frac{\alpha}{\lambda^2} \tag{A.3}$$

Appendix B

Lang-Kobayashi Equations[54,104,110] describes the dynamics in a single mode semiconductor laser diode with optical feedback reflected from a remote target:

$$\frac{dE(t)}{dt} = \frac{1}{2}\left[G_n(N(t) - N_0) - \frac{1}{\tau_p} \right] E(t) + \frac{\kappa}{\tau_c} E(t-\tau)\cos[\omega_0 \tau + \phi(t) - \phi(t-\tau)] \quad \text{(B.1a)}$$

$$\frac{d\phi(t)}{dt} = \frac{1}{2}\alpha G_n(N(t) - N_{th}) - \frac{\kappa}{\tau_c}\frac{E(t-\tau)}{E(t)}\sin[\omega_0 \tau + \phi(t) - \phi(t-\tau)] \quad \text{(B.1b)}$$

$$\frac{dN(t)}{dt} = G_{gen} - \frac{N(t)}{\tau_e} - G_n[N(t) - N_0]E^2(t) \quad \text{(B.1c)}$$

In the above equations, the meaning of the symbols are listed below:

$E(t)$ - normalized slowly-varying envelope of the electric field where $E(t)^2 \propto$ photon density.

$\phi(t)$ - phase of the electric field

ω_0 - angular frequency of the laser emission without optical feedback.

G_n - modal gain coefficient

G_{gen} - electrical pumping term

N_0 - carrier density at transparency

$N(t)$ - spatial averaged carrier concentration

N_{th} - carrier density at laser threshold

τ_e - carrier lifetime

τ_c - photon intra-cavity round trip time $\frac{2 \cdot n \cdot l}{c}$

τ - photon external cavity round trip time $\frac{2 \cdot L}{c}$

τ_p - photon lifetime in the cavity. $\tau_p^{-1} = G_n \times (N_{th} - N_0)$.

α - linewidth enhancement factor

κ - coupling coefficient between intra-cavity light and the optical feedback. Given by Equation (6.3)

Stationary solution can be found when the first derivative of the intra-cavity electric field and carrier density equal to zero. In other words, in Equation (B.1a) and (B.1c), $\frac{dE(t)}{dt} = 0$ and $\frac{dN(t)}{dt} = 0$. And thus we also have $E(t) = E(t-\tau)$ and $N(t) = N_F$. The instantaneous frequency with optical feedback can be expressed as $\omega_F(\tau)$. By plugging $\phi(t) = (\omega_F(\tau) - \omega_0)t$ into Equation (B.1a), it yields:

$$N_F = N_{th} - \frac{2\kappa}{G_n \tau_c} \cos[\omega_F(\tau) \cdot \tau] \tag{B.2}$$

If we substitute the *N(t)* with the above N_F expression in phase equation Equation (B.1b), we will obtain:

$$\omega_F(\tau) = \omega_0 - \frac{\kappa}{\tau_c} \{\alpha \cdot \cos[\omega_F(\tau) \cdot \tau] + \sin[\omega_F(\tau) \cdot \tau]\} \tag{B.3}$$

By using the definition of C parameter in Equation (6.2), we will deduce the expression for $\omega_F(\tau)$ in Equation (6.4), which is an implicit function of τ, the external-cavity round-trip time.

Bibliography

1. Dazzi, A., Prazeres, R., Glotin, F. & Ortega, J. M. Local infrared microspectroscopy with subwavelength spatial resolution with an atomic force microscope tip used as a photothermal sensor. *Opt. Lett.* **30,** 2388–2390 (2005).
2. Huth, F., Schnell, M., Wittborn, J., Ocelic, N. & Hillenbrand, R. Infrared-spectroscopic nanoimaging with a thermal source. *Nat. Mater.* **10,** 352–6 (2011).
3. Huth, F. *et al.* Nano-FTIR absorption spectroscopy of molecular fingerprints at 20 nm spatial resolution. *Nano Lett.* **12,** 3973–3978 (2012).
4. Huth, F. *et al.* Resonant antenna probes for tip-enhanced infrared near-field microscopy. *Nano Lett.* **13,** 1065–1072 (2013).
5. Hillenbrand, R., Taubner, T. & Keilmann, F. Phonon-enhanced light matter interaction at the nanometre scale. *Nature* **418,** 159–162 (2002).
6. Bailo, E. & Deckert, V. Tip-enhanced Raman spectroscopy of single RNA strands: Towards a novel direct-sequencing method. *Angew. Chemie - Int. Ed.* **47,** 1658–1661 (2008).
7. Schmid, T., Yeo, B.-S., Leong, G., Stadler, J. & Zenobi, R. Performing tip-enhanced Raman spectroscopy in liquids. *J. Raman Spectrosc.* **40,** 1392–1399 (2009).
8. Deckert, V. Tip-enhanced raman spectroscopy. *J. Raman Spectrosc.* **40,** 1336–1337 (2009).
9. Lahiri, B., Holland, G. & Centrone, A. Chemical imaging beyond the diffraction limit: experimental validation of the PTIR technique. *Small* **9,** 439–45 (2013).
10. Jin, M., Lu, F. & Belkin, M. A. High sensitivity infrared vibrational nanospectroscopy in water. *Light Sci. Appl.* (2017).
11. Nie, S. & Emory, S. R. Probing single molecules and single nanoparticles by surface-enhanced Raman scattering. *Science (80-.).* **275,** 1102–1106 (1997).
12. Kneipp, K., Wang, Y., Kneipp, H., Perelman, L. T. & Itzkan, I. Single molecule detection using surface-enhanced Raman scattering (SERS). *Phys. Rev. …* **78,** 1667–1670 (1997).
13. Kneipp, K. & Kneipp, H. Single Molecule Raman Scattering. *Appl. Spectrosc.* **60,** 322A–334A (2006).
14. Binnig, G., Rohrer, H., Gerber, C. & Weibel, E. Surface studies by scanning tunneling microscopy. *Phys. Rev. Lett.* **49,** 57–61 (1982).
15. Binnig, G., Rohrer, H., Gerber, C. & Weibel, E. 7 × 7 Reconstruction on Si(111) Resolved in Real Space. *Phys. Rev. Lett.* **50,** 120–123 (1983).
16. Binnig, G. & Quate, C. F. Atomic Force Microscope. *Phys. Rev. Lett.* **56,** 930–933 (1986).
17. Betzig, E., Lewis, A., Harootunian, A., Isaacson, M. & Kratschmer, E. Near-field scanning optical microscopy (NSOM). *Biophys. J.* **49,** 269–279 (1986).
18. Dürig, U., Pohl, D. W. & Rohner, F. Near-field optical-scanning microscopy. *J.*

Appl. Phys. **59,** 3318–3327 (1986).
19. Pohl, D. W., Denk, W. & Lanz, M. Optical stethoscopy: Image recording with resolution λ/20. *Appl. Phys. Lett.* **44,** 651–653 (1984).
20. Lewis, A., Isaacson, M., Harootunian, A. & Muray, A. Development of a 500 Å spatial resolution light microscope: I. light is efficiently transmitted through λ/16 diameter apertures. *Ultramicroscopy* **13,** 227–231 (1984).
21. Jordan, C. E., Stranick, S. J., Cavanagh, R. R., Richter, L. J. & Chase, D. B. Near-Field Scanning Optical Microscopy Incorporating Raman Scattering for Vibrational Mode Contrast. *Surf. Sci.* **435,** 48–52 (1999).
22. Hong, M. K. *et al.* Imaging single living cells with a scanning near-field infrared microscope based on a free electron laser. *Nucl. Instruments Methods Phys. Res. Sect. B Beam Interact. with Mater. Atoms* **144,** 246–255 (1998).
23. Michaels, C. A., Stranick, S. J., Richter, L. J. & Cavanagh, R. R. Scanning near-field infrared microscopy and spectroscopy with a broadband laser source. *J. Appl. Phys.* **88,** 4832–4839 (2000).
24. Piednoir, A., Creuzet, F., Licoppe, C. & Ortéga, J. M. Locally resolved infrared spectroscopy. *Ultramicroscopy* **57,** 282–286 (1995).
25. De Wilde, Y., Lemoine, P. A. & Babuty, A. Near-Field Optical Microscopy in the Infrared Range. *Top. Appl. Phys.* **118,** 439–467 (2009).
26. Platkov, M., Tsun, A., Nagli, L. & Katzir, A. A scanning near-field middle-infrared microscope for the study of objects submerged in water. *Appl. Phys. Lett.* **92,** 10–13 (2008).
27. Gheber, L. A., Hwang, J. & Edidin, M. Design and optimization of a near-field scanning optical microscope for imaging biological samples in liquid. *Appl. Opt.* (2000).
28. Kawata, S. & Inouye, Y. Scanning probe optical microscopy using a metallic probe tip. *Ultramicroscopy* **57,** 313–317 (1995).
29. Zenhausern, F. M., Boyle, M. P. O. ' & Wickramasingha, H. K. Apertureless near-field optical microscope. *Appl. Phys. Lett.* **65,** 1623–1625 (1994).
30. Wessel, J. Surface-enhanced optical microscopy. *J. Opt. Soc. Am. B* **2,** 1538–1541 (1985).
31. Knoll, B. & Keilmann, F. Scanning microscopy by mid-infrared near-field scattering. *Appl. Phys. A Mater. Sci. Process.* **66,** 477–481 (1998).
32. Knoll, B. & Keilmann, F. Enhanced dielectric contrast in scattering-type scanning near-field optical microscopy. *Opt. Commun.* **182,** 321–328 (2000).
33. Hillenbrand, R., Knoll, B. & Keilmann, F. Pure optical contrast in scattering-type scanning near-field microscopy. *J. Microsc.* **202,** 77–83 (2001).
34. Raschke, M. B. *et al.* Apertureless near-field vibrational imaging of block-copolymer nanostructures with ultrahigh spatial resolution. *ChemPhysChem* **6,** 2197–2203 (2005).
35. Sasaki, Y. & Sasaki, H. Heterodyne Detection for the Extraction of the Probe-

Scattering Signal in Scattering-Type Scanning Near-Field Optical Microscope Heterodyne Detection for the Extraction of the Probe-Scattering Signal in Scattering-Type Scanning Near-Field Optical Microsco. *Jpn. J. Appl. Phys.* **39,** 321–323 (2000).

36. Taubner, T., Hillenbrand, R. & Keilmann, F. Performance of visible and mid-infrared scattering-type near-field optical microscopes. *J. Microsc.* **210,** 311–314 (2003).
37. Xu, X. G., Rang, M., Craig, I. M. & Raschke, M. B. Pushing the sample-size limit of infrared vibrational nanospectroscopy: From monolayer toward single molecule sensitivity. *J. Phys. Chem. Lett.* **3,** 1836–1841 (2012).
38. Chen, J. *et al.* Optical nano-imaging of gate-tunable graphene plasmons. *Nature* **487,** 77–81 (2012).
39. Fei, Z. *et al.* Gate-tuning of graphene plasmons revealed by infrared nano-imaging. *Nature* **486,** 82–85 (2012).
40. Lu, F. & Belkin, M. A. Infrared absorption nano-spectroscopy using sample photoexpansion induced by tunable quantum cascade lasers. *Opt. Express* **19,** 19942 (2011).
41. Lu, F., Jin, M. & Belkin, M. a. Tip-enhanced infrared nanospectroscopy via molecular expansion force detection. *Nat. Photonics* **8,** 307–312 (2014).
42. Stöckle, R. M., Suh, Y. D., Deckert, V. & Zenobi, R. Nanoscale chemical analysis by tip-enhanced Raman spectroscopy. *Chem. Phys. Lett.* **318,** 131–136 (2000).
43. Wang, J. J. *et al.* Apertureless near-field Raman spectroscopy. *J. Microsc.* **210,** 330–333 (2003).
44. Anderson, M. S. Locally enhanced Raman spectroscopy with an atomic force microscope. *Appl. Phys. Lett.* **76,** 3130–3132 (2000).
45. Zhang, R. *et al.* Chemical mapping of a single molecule by plasmon-enhanced Raman scattering. *Nature* **498,** 82–86 (2013).
46. Dazzi, a, Prazeres, R., Glotin, F. & Ortega, J. M. Local infrared microspectroscopy with subwavelength spatial resolution with an atomic force microscope tip used as a photothermal sensor. *Opt. Lett.* **30,** 2388–2390 (2005).
47. Mayet, C. *et al.* Sub-100 nm IR spectromicroscopy of living cells. *Opt. Lett.* **33,** 1611–3 (2008).
48. Ramer, G., Ruggeri, F. S., Levin, A., Knowles, T. P. J. & Centrone, A. Determination of Polypeptide Conformation with Nanoscale Resolution in Water. *ACS Nano* **12,** 6612–6619 (2018).
49. Lahiri, B., Holland, G., Aksyuk, V. & Centrone, A. Nanoscale imaging of plasmonic hot spots and dark modes with the photothermal-induced resonance technique. *Nano Lett.* **13,** 3218–3224 (2013).
50. Yum, K., Wang, Z., Suryavanshi, A. P. & Yu, M.-F. Experimental measurement and model analysis of damping effect in nanoscale mechanical beam resonators in air. *J. Appl. Phys.* **96,** 3933 (2004).

51. Nowak, D. *et al.* Nanoscale chemical imaging by photoinduced force microscopy. *Sci. Adv.* **2,** (2016).
52. Wang, L. *et al.* Nanoscale simultaneous chemical and mechanical imaging via peak force infrared microscopy. *Sci. Adv.* **3,** 1–12 (2017).
53. Giuliani, G., Norgia, M., Donati, S. & Bosch, T. Laser diode self-mixing technique for sensing applications. *J. Opt. A Pure Appl. Opt.* **4,** S283–S294 (2002).
54. Guiliani, G. & Donati, S. in *Unlocking Dynamical Diversity: Optical Feedback Effects on Semiconductor Lasers* 217–253 (2005).
55. Donati, S. & Fellow, L. Responsivity and Noise of Self-Mixing Photodetection Schemes. **47,** 1428–1433 (2011).
56. Dean, P. *et al.* Terahertz imaging through self-mixing in a quantum cascade laser Paul. *Opt. Lett.* **36,** 2587–2588 (2012).
57. Valavanis, A. *et al.* Self-Mixing Interferometry With Terahertz Quantum Cascade Lasers. *IEEE Sens. J.* **13,** 37–43 (2013).
58. Dean, P. *et al.* Apertureless near-field terahertz imaging using the self-mixing effect in a quantum cascade laser. *Appl. Phys. Lett.* **108,** (2016).
59. Keeley, J. *et al.* Measurement of the emission spectrum of a semiconductor laser using laser-feedback interferometry. *Sci. Rep.* **7,** 1–9 (2017).
60. Giordano, M. C. *et al.* Phase-resolved terahertz self-detection near- field microscopy. *Opt. Express* **26,** 18423–18435 (2018).
61. Giordano, M. C., Viti, L., Mitrofanov, O. & Vitiello, M. S. Phase-sensitive terahertz imaging using room-temperature near-field nanodetectors. *Optica* **5,** 651–657 (2018).
62. Katharina Von Puttkamer, Hans-Rolf Dubal, M. Q. Time-dependent Processes in Polyatomic Molecules During and After Intense Infrared Irradiation. *Faraday Discuss. Chem. Soc.* **75,** 197–210 (1983).
63. Derjaguin, B. V, Muller, V. M. & Toporov, Y. U. P. Effect of contact deformation on the adhesion of particles. *J. Colloid Interface Sci.* **52,** 105–108 (1975).
64. Delrio, F. W., Jaye, C., Fischer, D. A. & Cook, R. F. Elastic and adhesive properties of alkanethiol self-assembled monolayers on gold. *Appl. Phys. Lett.* **94,** 10–13 (2009).
65. Rabe, U., Janser, K. & Arnold, W. Vibrations of free and surface-coupled atomic force microscope cantilevers: Theory and experiment. *Rev. Sci. Instrum.* **67,** 3281 (1996).
66. Dazzi, A., Glotin, F. & Carminati, R. Theory of infrared nanospectroscopy by photothermal induced resonance. *J. Appl. Phys.* **107,** (2010).
67. Felts, J. R. *et al.* Atomic force microscope infrared spectroscopy on 15 nm scale polymer nanostructures. *Rev. Sci. Instrum.* **84,** (2013).
68. Troccoli, M. *et al.* High-performance quantum cascade lasers grown by metal-organic vapor phase epitaxy and their applications to trace gas sensing. *J. Light. Technol.* **26,** 3534–3555 (2008).

69. Love, J. C., Estroff, L. a., Kriebel, J. K., Nuzzo, R. G. & Whitesides, G. M. *Self-Assembled Monolayers of Thiolates on Methals as a Form of Nanotechnology*. *Chem. Rev.* (2005). doi:10.1021/cr0300789
70. Hegner, M., Wagner, P. & Semenza, G. Ultralarge atomically flat template-stripped Au surfaces for scanning probe microscopy. *Surf. Sci.* **291,** 39–46 (1993).
71. Harder, P., Grunze, M., Dahint, R., Whitesides, G. M. & Laibinis, P. E. Molecular Conformation in Oligo(ethylene glycol)-Terminated Self-Assembled Monolayers on Gold and Silver Surfaces Determines Their Ability To Resist Protein Adsorption. *J. Phys. Chem. B* **102,** 426–436 (1998).
72. Merklin, G. T., He, L. & Griffiths, P. R. Surface-Enhanced Infrared Absorption Spectrometry of p-Nitrothiophenol and its Disulfide. *Appl. Spectrosc.* **53,** 4–9 (1999).
73. Yeo, B.-S., Stadler, J., Schmid, T., Zenobi, R. & Zhang, W. Tip-enhanced Raman Spectroscopy – Its status, challenges and future directions. *Chem. Phys. Lett.* **472,** 1–13 (2009).
74. Khatib, O. *et al.* Graphene-Based Platform for Infrared Near-Field Nanospectroscopy of Water and Biological Materials in an Aqueous Environment. *ACS Nano* **9,** 7968–75 (2015).
75. Hansen, W. N. Electric Fields Produced by the Propagation of Plane Coherent Electromagnetic Radiation in a Stratified Medium. *J. Opt. Soc. Am.* **58,** 380 (1968).
76. Inouye, Y. & Kawata, S. Near-field scanning optical microscope with a metallic probe tip. *Opt. Lett.* **19,** 159 (1994).
77. Max, J. J. & Chapados, C. Isotope effects in liquid water by infrared spectroscopy. III. H 2O and D2O spectra from 6000 to 0 cm-1. *J. Chem. Phys.* **131,** 0–13 (2009).
78. Cleveland, J. P., Ohnesorge, F., Walters, D. A., Hansma, P. K. & Scha, T. E. Studies of vibrating atomic force microscope cantilevers in liquid. *J. Appl. Phys.* **80,** 3622–3627 (1996).
79. Höppener, C., Siebrasse, J. P., Peters, R., Kubitscheck, U. & Naber, a. High-resolution near-field optical imaging of single nuclear pore complexes under physiological conditions. *Biophys. J.* **88,** 3681–8 (2005).
80. Van Eysden, C. & Sader, J. E. Resonant frequencies of a rectangular cantilever beam immersed in a fluid. *J. Appl. Phys.* **100,** 114916 (2006).
81. Sader, J. E., Chon, J. W. M. & Mulvaney, P. Calibration of rectangular atomic force microscope cantilevers. *Rev. Sci. Instrum.* **70,** 3967 (1999).
82. Chon, J. W. M., Mulvaney, P. & Sader, J. E. Experimental validation of theoretical models for the frequency response of atomic force microscope cantilever beams immersed in fluids. *J. Appl. Phys.* **87,** 3978 (2000).
83. Sader, J. E. Frequency response of cantilever beams immersed in viscous fluids with applications to the atomic force microscope. *J. Appl. Phys.* **84,** 64 (1998).
84. Salaita, K., Wang, Y. & Mirkin, C. a. Applications of dip-pen nanolithography. *Nat. Nanotechnol.* **2,** 145–155 (2007).

85. Shin, Y. H. *et al.* Polymer-coated tips for patterning of viruses by dip-pen nanolithography. *Angew. Chemie - Int. Ed.* **49,** 9689–9692 (2010).
86. Dinelli, F., Menozzi, C., Baschieri, P., Facci, P. & Pingue, P. Scanning probe nanoimprint lithography. *Nanotechnology* **21,** 75305 (2010).
87. Mtller, W. T. *et al.* A Strategy for the Chemical Synthesis of Nanostructures. *Science (80-.).* **268,** 272–273 (1995).
88. Péter, M., Li, X. M., Huskens, J. & Reinhoudt, D. N. Catalytic probe lithography: Catalyst-functionalized scanning probes as nanopens for nanofabrication on self-assembled monolayers. *J. Am. Chem. Soc.* **126,** 11684–11690 (2004).
89. Gross, L. *et al.* only appears when looking at the I. *Science (80-.).* **325,** 1110–4 (2009).
90. Nobile, C. *et al.* Probe tips functionalized with colloidal nanocrystal tetrapods for high-resolution atomic force microscopy imaging. *Small* **4,** 2123–2126 (2008).
91. Dai, H., Hafner, J. H., Rinzler, A. G., Colbert, D. T. & Smalley, R. E. Nanotubes as nanoprobes in scanning probe microscopy. *Nature* **384,** 147–150 (1996).
92. Cameron, N. S., Ott, A., Roberge, H. & Veres, T. Chemical force microscopy for hot-embossing lithography release layer characterization. *Soft Matter* **2,** 553–557 (2006).
93. Noy, A., Vezenov, D. V. & Lieber, C. M. Chemical Force Microscopy. *Annu. Rev. Mater. Sci.* **27,** 381–421 (1997).
94. Frisbie, C. D., Rozsnyai, L. F., Aleksandr, N., Wrighton, M. S. & Lieber, C. M. Functional group imaging by Chemical Force Microscopy. *Science (80-.).* **265,** 2071–2074 (1994).
95. Lee, G. U., Kidwell, D. A. & Colton, R. J. Sensing Discrete Streptavidin Biotin Interactions With Atomic-Force Microscopy. *Langmuir* **10,** 354–357 (1994).
96. Ludwig, M., Dettmann, W. & Gaub, H. E. Atomic force microscope imaging contrast based on molecular recognition. *Biophys. J.* **72,** 445–8 (1997).
97. Stipe, B. C., Rezaei, M. A. & Ho, W. Single-molecule vibrational spectroscopy and microscopy. *Science (80-.).* **280,** 1732–1735 (1998).
98. Bortchagovsky, E. G., Fischer, U. C. & Schmid, T. Possibilities of functionalized probes in optical near-field microscopy. *Phys. Scr.* **T162,** 014005 (2014).
99. Bortchagovsky, E. G. & Fischer, U. C. A tetrahedral tip as a probe for tip-enhanced Raman scattering and as a near-field Raman probe. *J. Raman Spectrosc.* **40,** 1386–1391 (2009).
100. Trager, F., Coufal, H. & Chuang, T. J. with Silver Films. *Phys. Rev. Lett.* **49,** 1720–1723 (1982).
101. Bras, A. W. *et al.* Simultaneous Studies of Reaction Kinetics and Structure Development in Polymer Processing. *Science (80-.).* **267,** 996–999 (1995).
102. Ylgor, E., Ylgor, I. & Yurtsever, E. Hydrogen bonding and polyurethane morphology. I. Quantum mechanical calculations of hydrogen bond energies and vibrational spectroscopy of model compounds. *Polymer (Guildf).* **43,** 6551–6559

(2002).
103. Boland, T. & Ratner, B. D. Direct measurement of hydrogen bonding in DNA nucleotide bases by atomic force microscopy. *Proc. Natl. Acad. Sci. U. S. A.* **92,** 5297–5301 (1995).
104. Mezzapesa, F. *et al.* Intrinsic stability of quantum cascade lasers against optical feedback. *Opt. Express* **21,** 13748–57 (2013).
105. Mezzapesaa, F. P. *et al.* Coherent imaging with mid-IR and THz quantum cascade lasers through optical feedback interferometry. 0–3 (2013).
106. Raschke, M. B. & Lienau, C. Apertureless near-field optical microscopy: Tip-sample coupling in elastic light scattering. *Appl. Phys. Lett.* **83,** 5089–5091 (2003).
107. Beck, M. *et al.* Continuous Wave operation of Mid-Infrared Simoconductor Laser at Room Temperature. *Science (80-.).* **295,** 301–305 (2002).
108. Villares, G. *et al.* On-chip Dual-comb based on Quantum Cascade Laser Frequency Combs. *Appl. Phys. Lett.* **251104,** 1–5 (2015).
109. Villares, G., Hugi, A., Blaser, S. & Faist, J. Dual-comb spectroscopy based on quantum-cascade-laser frequency combs. *Nat. Commun.* **5,** 5192 (2014).
110. Lang, R. & Kobayashi, K. External Optical Feedback Effects on Semiconductor Injection Laser Properties. *IEEE J. Quantum Electron.* **16,** 347–355 (1980).
111. Hillenbrand, R. & Keilmann, F. Complex optical constants on a subwavelength scale. *Phys. Rev. Lett.* **85,** 3029–3032 (2000).
112. Ocelic, N., Huber, A. & Hillenbrand, R. Pseudoheterodyne detection for background-free near-field spectroscopy. *Appl. Phys. Lett.* **89,** (2006).
113. Keilmann, F. & Hillenbrand, R. Near-field microscopy by elastic light scattering from a tip. *Philos. Trans. A. Math. Phys. Eng. Sci.* **362,** 787–805 (2004).
114. Cvitkovic, A., Ocelic, N. & Hillenbrand, R. Analytical model for quantitative prediction of material contrasts in scattering-type near-field optical microscopy. *Opt. Express* **15,** 8550 (2007).
115. Khurgin, J. B., Dikmelik, Y., Hugi, A. & Faist, J. Coherent frequency combs produced by self frequency modulation in quantum cascade lasers. *Appl. Phys. Lett.* **104,** (2014).
116. Bartalini, S. *et al.* Frequency-comb-assisted terahertz quantum cascade laser spectroscopy. *Phys. Rev. X* **4,** 1–7 (2014).
117. Friedli, P. *et al.* Four-wave mixing in a quantum cascade laser amplifier. *Appl. Phys. Lett.* **102,** 2–6 (2013).
118. Lu, Q. Y. *et al.* High power frequency comb based on mid-infrared quantum cascade laser at $\lambda \sim 9$ μm.pdf.
119. Jouy, P. *et al.* Dual comb operation of $\lambda \sim 8.2$ μ m quantum cascade laser frequency comb with 1 W optical power. *Appl. Phys. Lett.* **111,** 2–6 (2017).
120. Burghoff, D. *et al.* Terahertz laser frequency combs. *Nat. Photonics* **8,** 462–467 (2014).
121. Bohren, C. F. & Huffman, D. R. *Absorption and Scattering of Light by Small*

Particles. *John Wiley & Sons, Inc* (1983). doi:10.1080/716099663